Regional-scale airborne electromagnetic surveying of the Yucatan karst aquifer (Mexico): geological and hydrogeological interpretation

Bibi R. N. Gondwe, David Ottowitz, Robert Supper, Klaus Motschka, Gonzalo Merediz-Alonso & Peter Bauer-Gottwein

Hydrogeology Journal
Official Journal of the International Association of Hydrogeologists

ISSN 1431-2174

Hydrogeol J
DOI 10.1007/s10040-012-0877-8

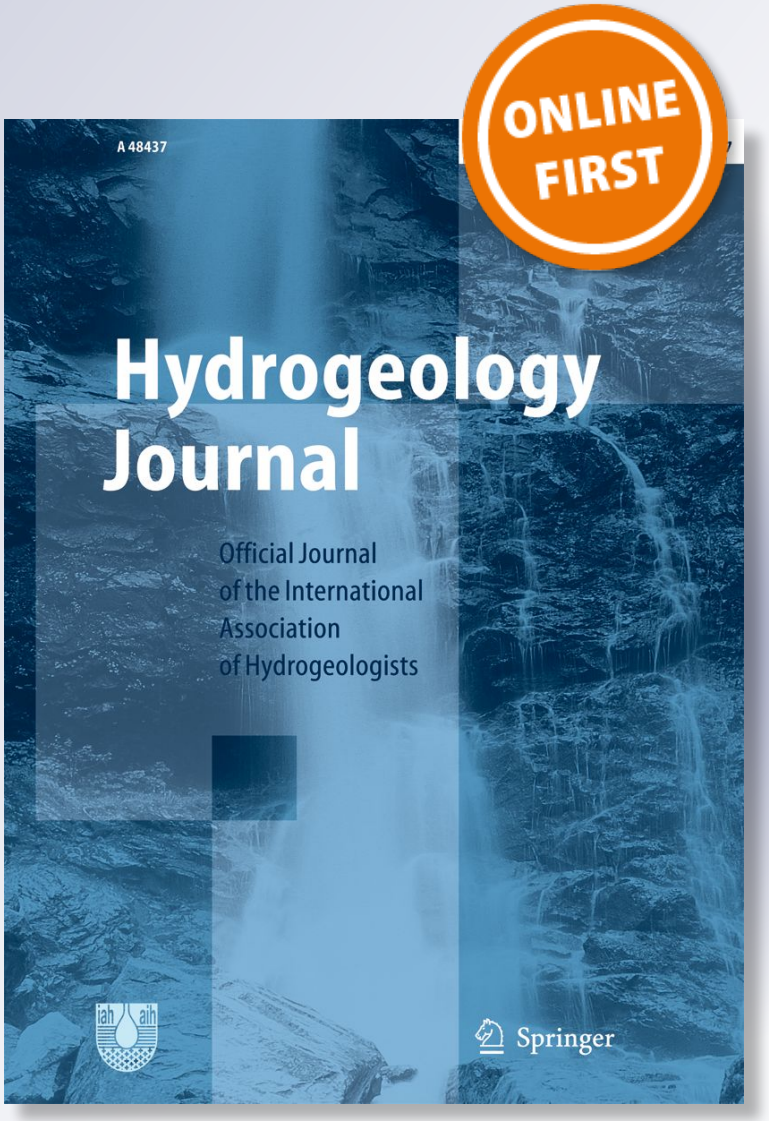

Springer

Regional-scale airborne electromagnetic surveying of the Yucatan karst aquifer (Mexico): geological and hydrogeological interpretation

Bibi R. N. Gondwe · David Ottowitz · Robert Supper · Klaus Motschka · Gonzalo Merediz-Alonso · Peter Bauer-Gottwein

Abstract Geometry and connectivity of high-permeability zones determine groundwater flow in karst aquifers. Efficient management of karst aquifers requires regional mapping of preferential flow paths. Remote-sensing technology provides tools to efficiently map the subsurface at such scales. Multi-spectral remote sensing imagery, shuttle radar topography data and frequency-domain airborne electromagnetic (AEM) survey data were used to map karst-aquifer structure on the Yucatan Peninsula, Mexico. Anomalous AEM responses correlated with topographic features and anomalous spectral reflectance of the terrain. One known preferential flow path, the Holbox fracture zone, showed lower bulk electrical resistivity than its surroundings in the AEM surveys. Anomalous structures delineated inland were sealed above by a low-resistivity layer (resistivity: 1–5 Ωm, thickness: 5–6m). This layer was interpreted as ejecta from the Chicxulub impact (Cretaceous/Paleogene boundary), based on similar resistivity signatures found in borehole logs. Due to limited sensitivity of the AEM survey, the subsurface configuration beneath the low-resistivity layer could not be unambiguously determined. AEM measurements combined with remote-sensing data analysis provide a potentially powerful multi-scale methodology for structural mapping in karst aquifers on the Yucatan Peninsula and beyond.

Keywords Remote sensing · Frequency-domain EM · Karst · Yucatan · Mexico

Received: 22 February 2011 / Accepted: 21 May 2012

B. R. N. Gondwe (✉) · P. Bauer-Gottwein
Department of Environmental Engineering,
Technical University of Denmark,
Miljoevej, Building 113, 2800 Kgs. Lyngby, Denmark
e-mail: bibi.neuman@gmail.com
Tel.: +45-4525-2228
Fax: +45-4593-2850

P. Bauer-Gottwein
e-mail: pbau@env.dtu.dk

D. Ottowitz · R. Supper · K. Motschka
Geological Survey of Austria,
Neulinggasse 38, 1030 Vienna, Austria

D. Ottowitz
e-mail: david.ottowitz@geologie.ac.at

R. Supper
e-mail: robert.supper@geologie.ac.at

K. Motschka
e-mail: klaus.motschka@geologie.ac.at

G. Merediz-Alonso
Amigos de Sian Ka'an,
Fuego # 2, Manzana 10 SM 4, Cancún, Quintana Roo 77500
Mexico
e-mail: gmerediz@amigosdesiankaan.org

Introduction

Karst aquifers are extremely vulnerable to pollution. The high permeabilities of karst geology cause rapid infiltration, fast water flow through caves and limited retention of contaminants. Contaminant sequestration from caves to the matrix and subsequent slow release makes recovery from pollution events particularly slow for karst aquifers (Li et al. 2008). Karst aquifers provide the main source of water for about 20–25 % of the world's population (Ford and Williams 2007). The problem of karst groundwater protection is therefore globally relevant.

Delineating capture zones of well fields and groundwater-dependent ecosystems is a fundamental task in groundwater management. In karst aquifers, this task is particularly challenging because groundwater flow is heavily influenced by the geometry and connectivity of subsurface high-permeability structures such as caves and fracture zones. It is generally difficult to obtain information about such underground preferential flow paths, and to produce detailed descriptions of the complex heterogeneous subsurface of karst aquifers. Most karst aquifers may be conceptualized as double-continuum conduit-matrix media, with water exchange between the two domains (e.g. Peterson and Wicks 2005; Cornaton and

DOI 10.1007/s10040-012-0877-8

Published online: 13 June 2012

Perrochet 2002). Water storage and transport take place in both domains, but typically conduit flow dominates over matrix flow, while water storage is larger in the matrix than in the conduits (Atkinson 1977; Worthington 2003).

Remote-sensing data and geophysical methods have been successfully used to locate preferential flow paths and structures in karst aquifers; however, success of the various methods always depends on local site conditions (Benson and Yuhr 1993). Remote-sensing studies typically utilize optical imagery for creating lineament maps, either by visual inspection or using computer algorithms. Surface lineaments are commonly correlated with subsurface faults, fractures or conduits (e.g. Tam et al. 2005; Hung and Batelaan 2003; Süzen and Toprak 1998; Kresic 1995; Degirmenci and Günay 1992). Digital elevation models (DEM) have also been used to infer the location of subsurface karst features, because anomalies in geomorphology are often associated with karst structures (Masoud and Koike 2006).

In contrast to the terrain surface anomalies investigated with remote-sensing methods, geophysical exploration methods can detect subsurface anomalies. A wide variety of ground-based geophysical methods have been applied to locate subsurface karst features. The methods include microgravity (e.g. Mochales et al. 2008), magnetic resonance sounding (e.g. Vouillamoz et al. 2003), multielectrode resistivity imaging (e.g. Nyquist et al. 2007), seismics (e.g. Guérin et al. 2009), ground penetrating radar (e.g. Henson et al. 1997), very-low-frequency EM gradient surveys (e.g. Bosch and Müller 2005), and electromagnetic methods (e.g. Vogelsang 1987; Doolittle and Collins 1998; Shah et al. 2008). Geophysics has also been used to detect the main azimuth angles of subsurface high-permeability structures (e.g. Steinich and Marin 1997). The ground-based methods are applicable for local-scale studies. However, regional-scale studies require greater spatial coverage, and airborne electromagnetics (AEM) emerges as an attractive option in this context. The studies by Doll et al. (2000), Gamey et al. (2001), and Smith et al. (2005) successfully mapped general karst aquifer structure using AEM, and Supper et al. (2009) found excellent correlation between AEM anomalies and known karst conduit locations on the Yucatan Peninsula.

This study uses multi-spectral satellite imagery, digital elevation models (DEM) and AEM surveys to map regional-scale preferential flow paths in the Yucatan Peninsula (YP) karst aquifer. The YP is one of the world's largest and most spectacular karst aquifer systems. However, regional-scale groundwater flow on the YP is poorly understood, due to limited knowledge on the aquifer properties and their spatial variation. Bauer-Gottwein et al. (2011) have recently completed a comprehensive overview of the state of knowledge on the Yucatan karst aquifer. The study area is located in the eastern part of the YP (Fig. 1), and includes the Sian Ka'an Biosphere Reserve—a protected area with a groundwater-dependent wetland, which provides important ecosystem services and tourism revenue. The wetland seasonally varies in extent from approximately 1,000 to 2,600 km^2 (Gondwe et al. 2010b). The aquifer contains the world's longest submerged cave systems (QRSS 2010). Comprehensive coverage of the entire study area (35,000 km^2) with AEM was not feasible in this project. Therefore, multi-spectral imagery and DEM were used to locate potential high-permeability zones and structures in the regional karst aquifer. Some of these structures were subsequently targeted with AEM surveys. AEM results are interpreted in terms of their geological and hydrogeological significance.

Methods and data

A multi-scale approach was used to map karst aquifer structure on the YP at the regional scale. In a first step, multi-spectral satellite imagery and a digital elevation model were used to delineate potential high permeability zones at the scale of the entire study area (35,000 km^2). Subsequently, targeted AEM surveys were carried out over selected structures at the kilometer scale in order to clarify their geological and hydrogeological significance. This section provides an overview of the study area and the geological framework. Subsequently, the regional-scale mapping methods are presented. The section concludes with a description of the AEM surveys.

The study area

The study area is the conjectural groundwater capture zone of the wetland in the Sian Ka'an Biosphere Reserve, located in Quintana Roo, Mexico (Fig. 1). Previous hydrogeologic studies of the area are scarce (Perry et al. 2002, 2009; Beddows 2004). Gondwe et al. (2010a) present an integrated conceptual hydrogeologic model of the study area. The capture zone was delineated based on topographic divides and a few known groundwater flow divides. The groundwater heads available for the YP are in agreement with these tentative capture-zone boundaries (Gondwe et al. 2010a), while geochemical results of Perry et al. (2002) support the water divide at Lake Chichankanab. Average precipitation ranges from 840 to 1,550 mm/year, and groundwater recharge equals approximately 15 % of the rainfall (Gondwe et al. 2010a). The rainy season lasts from May to October. The aquifer hosts a thin freshwater lens (0–100 m thick) underlain by saltwater. Overall, the shape of the freshwater lens is in agreement with the Ghyben-Herzberg principle (Gondwe et al. 2010a; Marin et al. 2004; Steinich and Marin 1996; Moore et al. 1992). Soil thickness on the YP is limited and the predominant land cover is a 15–30-m-high semi-evergreen forest. The study area displays a notable topographic contrast. The topographic relief is flat in the northern and coastal part (elevations 0–20 m above mean sea level (mamsl)), whereas the south–southwestern portions have an undulating relief with cone-karst landforms (elevations up to 340 mamsl). These two geomorphologic zones are called the flat and the hilly area, respectively, in the remainder of this report (see Fig. 2a). A transition zone with moderately undulating relief (20–50 mamsl) is located between the flat and the hilly area.

 DOI 10.1007/s10040-012-0877-8

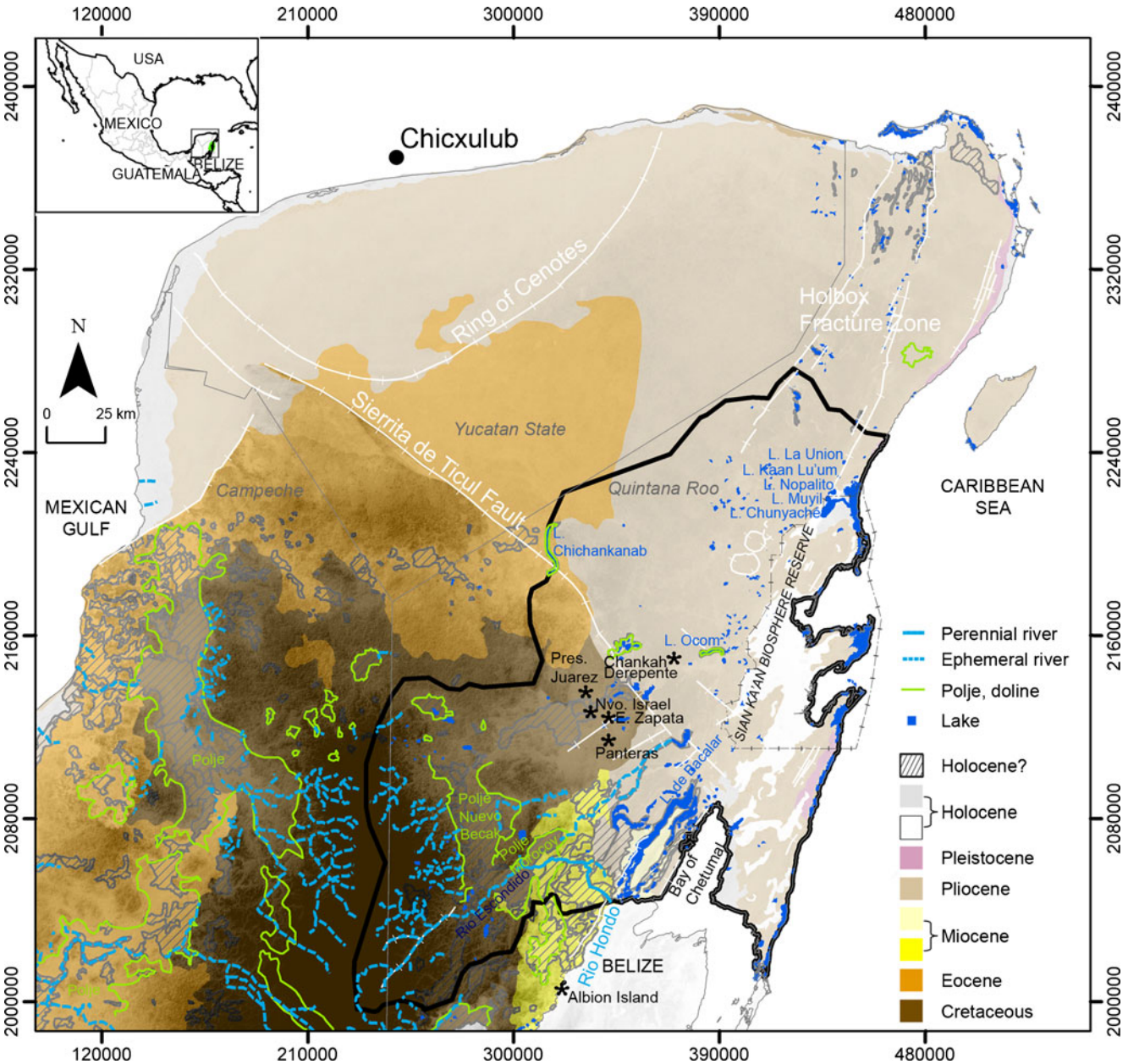

Fig. 1 Geology of the Yucatan peninsula, modified from SGM (2007). Topography from shuttle radar topography mission (SRTM; USGS 2006) overlain as grey-scaled transparent. Study area outlined with *thick black polygon*. *Dashed line* around *Sian Ka'an Biosphere Reserve* indicates boundary of the protected area. *Stars* indicate populated places. Coordinates are UTM zone 16 N, WGS84 datum and ellipsoid

Topographic depressions with seasonal swamps ('bajos', 'poljes') are found in the hilly area. Six of these depressions, were surveyed using AEM in this study, including the Holbox fracture zone. Seasonal surface drainage connects some of these swamps. Saline, undrained and/or waterlogged soils are found in some of the swampy areas. The hydrology of Sian Ka'an's wetlands was studied by Gondwe et al. (2010b). Further details on the study area are given in Gondwe et al. (2010a).

Geological framework

The YP consists of limestones, dolomites and evaporites reaching thicknesses of >1,500 m (Weidie, 1985). The surficial sedimentary rocks span Upper Cretaceous to Holocene in age, and are generally nearly horizontally layered and off-lapping, with gradually younger carbonates deposited towards the peninsula margins (Lopez-Ramos 1975; SGM 2007; Schönian et al. 2005). Kenkmann and Schönian (2006) emphasized that the geology of the southern peninsula is poorly constrained due to few exposures and difficulties in dating the sediments through biostratigraphy.

Ejecta associated with the Chicxulub meteorite impact, at the contact between Cretaceous and Paleogene sediments, has been found in southern Quintana Roo and neighboring Belize (Ocampo et al. 1996; Fouke et al. 2002; Pope et al. 2005; Schönian et al. 2005; Kenkmann

 DOI 10.1007/s10040-012-0877-8

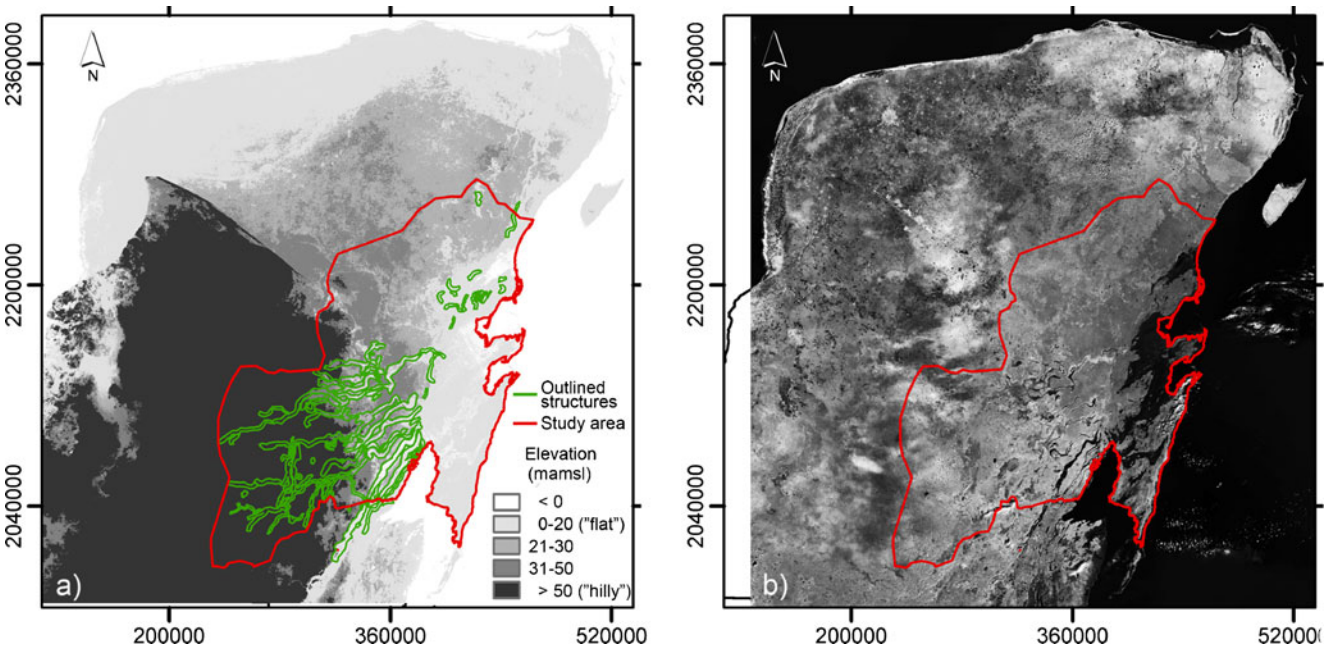

Fig. 2 **a** Topography from SRTM (USGS 2006), highlighting the hilly and the flat areas referred to in the text. Structures (*green*) outlined from visual inspection of satellite imagery are also shown. **b** Landsat Tri-Decadal TM mosaic band 4 (NASA 1990) in grey-scale, *white* indicating highest brightness. Structures are seen as *elongated black and white lines* in the southern-central part of the study area (*red*)

and Schönian 2006). The Chicxulub impact occurred in the northwestern YP (Hildebrand et al. 1991; Pope et al. 1991) at the approximate location of 21.3° N/89.5° W (NUTM16 (WGS84): 240600 mE, 2357400 mN), and a distance of about 80–350 km from the study area. Based on geochemical data, Perry et al. (2009) proposed that the ejecta blanket extends south and east of Lake Chichankanab. The extent of the possible ejecta blanket in the study area is not well known as Perry et al. (2009) only report on three water-sampling points in this region. The ejecta blanket is believed to be a discontinuous blanket, possibly due to erosion following its deposition (Pope et al. 2005; Kenkmann and Schönian 2006). In official geological maps some ejecta deposits in the hilly region appear to have been misdated to be Quaternary deposits, as some locations correlate with locations mapped by Kenkmann and Schönian (2006) as ejecta (Neuman and Rahbek 2007; Perry et al. 2009). The ejecta is expected to have a low permeability to water, as it is clay-rich, and has a sealing or partially sealing effect (Ocampo et al. 1996; Grajales-Nishimura et al. 2000; F. Schönian, Humboldt-Universität zu Berlin, pers. comm. 2007; Perry et al. 2009). Ground-based transient electromagnetic measurements and geophysical borehole logs reported in Gondwe et al. (2010a) show a geological unit with low resistivity and high natural gamma-radiation in the hilly area and the transition zone. The unit was generally encountered at around 0–13 m below surface (mbs) and was about 3–8 m thick. The unit was proposed to be the ejecta-layer (Gondwe et al. 2010a).

A series of sub-parallel faults, trending SSW–NNE exists in the southern part of the study area—The Río Hondo fault system. These faults have not been mapped in detail, but surface expressions are the fault-guided lakes in the study area, of which the largest is the ~54 km long Laguna de Bacalar. The fault system has also shaped the Caribbean coastline in the study area, and sub-parallel horst and graben systems are present offshore (Rosencrantz 1990). The Río Hondo fault system started forming in the late Jurassic, and continued to be active throughout the Cretaceous and Cenozoic. For this reason the rift structures are not hidden by sedimentary sequences (Dillon and Vedder 1973). Another fault system is located in the northern part of the study area—the Holbox fracture zone, also trending SSW–NNE. Its southern terminus is not well determined but possibly the Holbox and the Río Hondo fault systems intersect (Southworth 1985). Tulaczyk et al. (1993) described swales in the Holbox fractures zone as solution corridors, and mapped them based on remotely sensed optical and infrared imagery.

Regional-scale mapping using Landsat and Shuttle Radar Topography Mission (SRTM) data

Visual inspection of Landsat ETM+imagery revealed line-shaped features, resembling rivers, riverbeds or elongated structures on the land surface, which sometimes linked open water bodies. These structures were digitized manually. A nearly cloud-free true-color composite of the visual bands—RGB: band 3 (630–690 nm), band 2 (525–605 nm), band 1 (450–515 nm)—of Landsat ETM+ data (NASA Landsat Program 2000; 2001; 2002; please refer to the reference section for acquisition dates), and band 4 (near-infrared, 775–900 nm) from the Landsat TM Tri-Decadal mosaic (NASA Landsat Program 1990) were used, covering the entire study area. The spatial resolution of the imagery was 30 m×30 m. Band 4 displayed distinct very dark elongated structures within the study area west

 DOI 10.1007/s10040-012-0877-8

and southwest of Sian Ka'an. Low reflectance in band 4 typically indicates open water or high soil moisture. Figure 2b shows the peninsula imaged with band 4. Dark features can be clearly recognized in the central and southern part of the study area and around the northern swales of the Holbox fracture zone, while they are absent from the remainder of the YP. In the true-color composite, dark green river-like features (Fig. 2a) were identified in the central and southern part of the study area. Most of these features are not indicated on the most recent official map of perennial and ephemeral rivers (Fig. 1). Features with anomalous reflectance in either band 4 or in the true-color composite were manually digitized. Often the location of anomalous reflectance in band 4 coincided with the location of anomalous reflectance in the true-color composite. For display purposes, it was found that RGB combination of bands 2,3,1 with histogram stretching would at times enhance the river-like features for easier manual digitalization. Figure 3a–c display examples of some of the river-like features in the Landsat visual band composites and Landsat band 4. The corresponding land-surface elevation (Fig. 3d) and the structures digitized from the data (Fig. 3e) are also shown. For better visibility and to enable incorporation into a hydrologic model with grid size 1 km^2 (Gondwe et al. 2011), the identified structures were outlined with a 1.5–2.5-km-wide margin around them (Fig. 3e). Often this margin includes parts or all of the surrounding areas with a spectral signature that indicates wetlands or high soil moisture.

Topographic elevation data were obtained from the Shuttle Radar Topography Mission (SRTM, 90 m spatial resolution; USGS 2006). The SRTM dataset was resampled to 1 km × 1 km spatial resolution using an averaging filter. To investigate the spatial correlation between topographic depressions and the structures delineated from the multi-spectral imagery, DEM-based river delineation was performed with the software ILWIS 3.3 Academic (ITC 2005; Maathuis and Wang 2006). The algorithm consists of the following steps: (1) filling of internal depressions in the DEM; (2) computation of a flow direction map from the DEM; (3) computation of a flow accumulation map; (4) identification of river locations as pixels with flow accumulation values larger than a user-defined threshold. A threshold of 10,000 was used in this study. To test the stability of the river locations with respect to random errors in the DEM, the river delineation was repeated using a randomly perturbed DEM. A spatially uncorrelated random field of mean zero and standard deviation 10 m was added to the original DEM. The locations of the resulting delineated rivers were essentially unchanged.

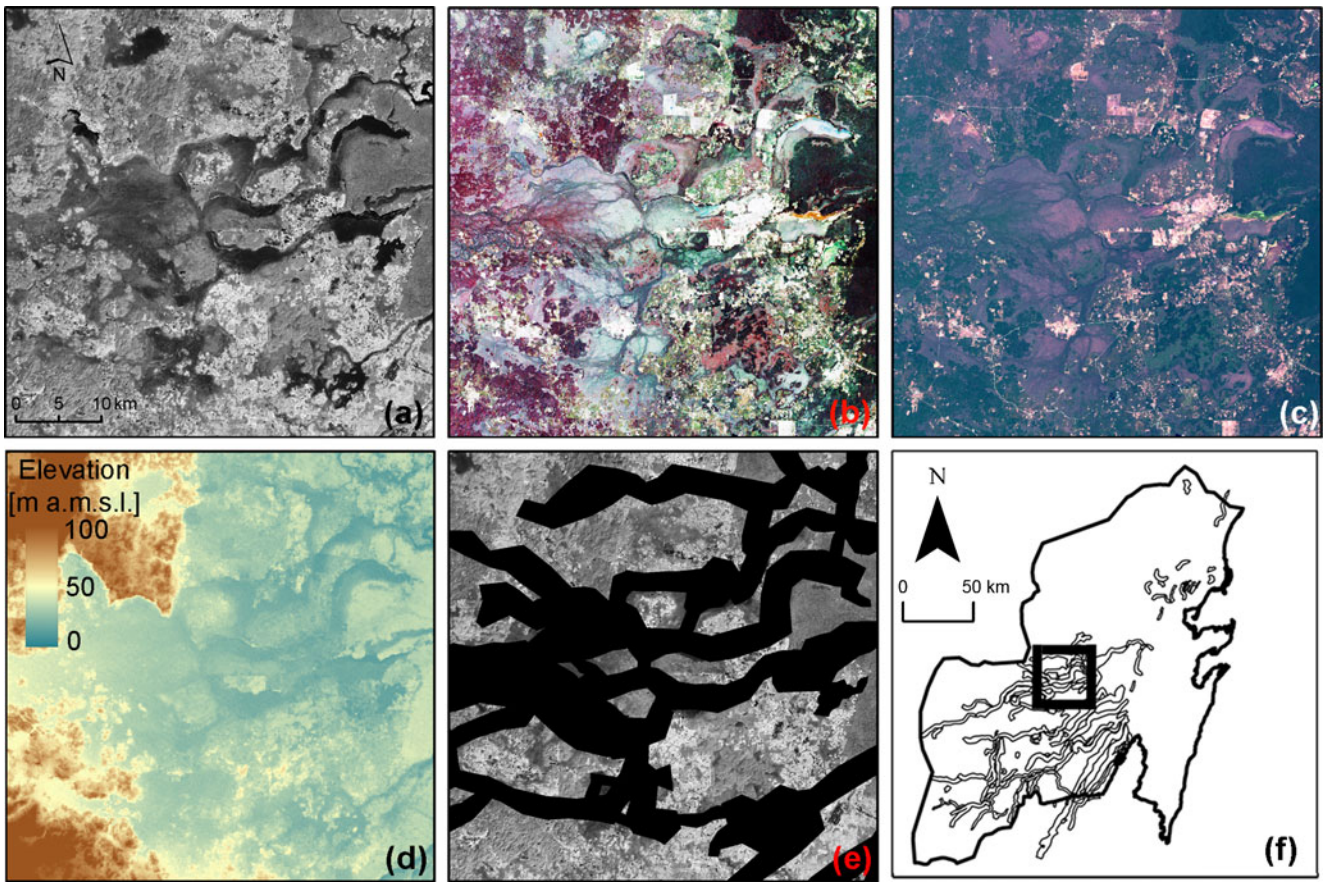

Fig. 3 Example of how the structures appear and have been mapped. **a** Landsat TM band 4, grayscale. *Bright* indicates high reflectance, **b** Landsat ETM+, RGB: band 2, band 3, band 1, histogram stretched, **c** Landsat ETM+true-color composite of visible bands (RGB=3,2,1), contrast and brightness enhanced for improved display, **d** topography from SRTM, **e** the delineated structures (*black areas*) displayed on Landsat ETM+band 4 for orientation, **f** Location of the mapped area

 DOI 10.1007/s10040-012-0877-8

Targeted airborne frequency-domain electromagnetic surveys – AEM

Targeted frequency-domain AEM surveys were flown over selected structures (Transects A–E, section 3.3) in the dry seasons of 2007 and 2008. Because of the relatively mild seasonality of precipitation, changes in the AEM data due to the season of acquisition are expected to be minor. The Geological Survey of Austria frequency-domain AEM system was used, consisting of a modified Geotech Hummingbird with four frequencies (340 Hz HCP, 3200 Hz VCX, 7190 Hz HCP and 28850 Hz VCX), four transmitter and four receiver coils in vertical co-axial (VCX) and horizontal coplanar (HCP) configuration. Motschka (2001) and Supper et al. (2009) provide further details on the equipment and data collection. Drift correction and data processing were carried out by the Geological Survey of Austria. The along-track sampling rate of the system is around 3 m, depending on the flight speed (typically around 80 km/h, ~44 knots). Frequency-domain AEM transmits a primary magnetic field at one or several given frequencies. The primary magnetic field induces eddy currents in the conductive subsurface. The eddy currents generate a secondary magnetic field, which is measured at the receiver (West and Macnae 1991). The skin depth (δ in meters) is the distance an EM wave will be reduced in amplitude by a factor of 1/e in a medium and depends on frequency and resistivity:

$$\delta = \sqrt{\frac{2\rho}{\mu\omega}} \approx 503 \cdot \sqrt{\frac{\rho}{\omega}} \qquad (1)$$

where ρ is the subsurface resistivity [Ω m], μ is the magnetic permeability, which, in sedimentary rocks, can be set equal to its free-space value of $4\pi \cdot 10^{-7}$ VsA^{-1} m^{-1} and ω is the angular frequency [rad/s] (West and Macnae 1991). Because the skin depth is a function of frequency, multiple-frequency frequency-domain AEM data provide better depth resolution compared to single frequency survey data. The subsurface resistivity distribution is obtained by fitting the simulated secondary magnetic field to the observed values. Assuming a layered earth structure (i.e. one-dimensional, 1D), this process is referred to as 1D inversion. Fitting parameters are the thicknesses and resistivities of the layered subsurface units (e.g. Zhdanov 2002 for 1D inversion, Avdeev 2005 for three-dimensional, 3D, inversion).

Subsurface electrical resistivity is correlated with the hydrogeological properties of the subsurface. One widely used empirical correlation for sediments and sedimentary rocks is Archie's Law (Archie 1942). Archie's Law reads:

$$\rho_f = \alpha \varphi^{-m} S_w^n \rho_w \qquad (2)$$

where ρ_f is the formation resistivity (or bulk resistivity, i.e. the property recovered in AEM) [Ωm], ρ_w is the resistivity of the porewater [Ωm], φ is the porosity of the rock or soil [dimensionless] and S_w is the water-filled fraction of the pore space [dimensionless], i.e. saturation. The parameters a, m and n are site specific and are determined empirically. Archie's Law is based on empirical observations from sedimentary rocks and its performance in karstic environments has not been thoroughly evaluated. However, it can be used to provide a rough idea of the porosity contrasts associated with variations in subsurface conductivity. Archie's Law implies that fracture zones and conduits containing fresh water in karst will have a lower formation resistivity than the surrounding unfractured limestone, because of their higher porosity. Moreover, saltwater-saturated media will have lower formation resistivity because of the reduced resistivity of the porewater compared to freshwater.

Karst geology with cave structures represents a 3D geophysical exploration target. Three-dimensional EM inversion to extract information on cave dimensions and depths currently was not attempted in this study. Hence the AEM data were analyzed using a qualitative anomaly mapping approach, similar to Supper et al. (2009). An AEM dataset for one space location consists of one ratio of the secondary to the primary magnetic fields (in [ppm]) for two orthogonal phase angles (referred to as "inphase" and "quadrature" components) and for each of the transmitted frequencies. Thus, for each space location, the AEM survey provides eight individual data points. Because AEM data are extremely sensitive to altitude, and because sensor altitude (h [m]) varied during the survey, a transform was applied to convert the measured signal into the response parameters M_i and N_i (both parts per million [ppm]) for each frequency i, which are much less sensitive to altitude than the untransformed measured signals (Huang 2008):

$$M_i = I_i \cdot \left(\frac{h}{s_i}\right)^3 \text{ and } N_i = Q_i \cdot \left(\frac{h}{s_i}\right)^3 \qquad (3)$$

where I_i are the inphase and Q_i the quadrature components of the untransformed signal for frequency i (both [ppm]), and s_i is the coil separation ([m]), which is different for different frequencies i.

For selected locations, 1D layered inversion of the AEM data was carried out using the 1D inversion software EM1DFM (UBC-GIF 2000). Twenty-five layers of exponentially increasing thickness to a depth of 30 m gave the best results. Below this depth, a homogeneous half-space was assumed.

In addition, forward modeling of the AEM signal over synthetic 1D and 3D subsurface resistivity models was performed using GeoTutor IV (PetroRos EiKon 2008). Prototypical subsurface resistivity models for the YP are shown in Fig. 4. In all models, the resistivity values of the geology were taken from Supper et al. (2009). Resistivity values of the fresh and saline groundwater are from Beddows (2004). Model A represents the typical background configuration where caves are not present, i.e. an unsaturated limestone layer is underlain by a limestone layer saturated with freshwater. This is underlain by a

 DOI 10.1007/s10040-012-0877-8

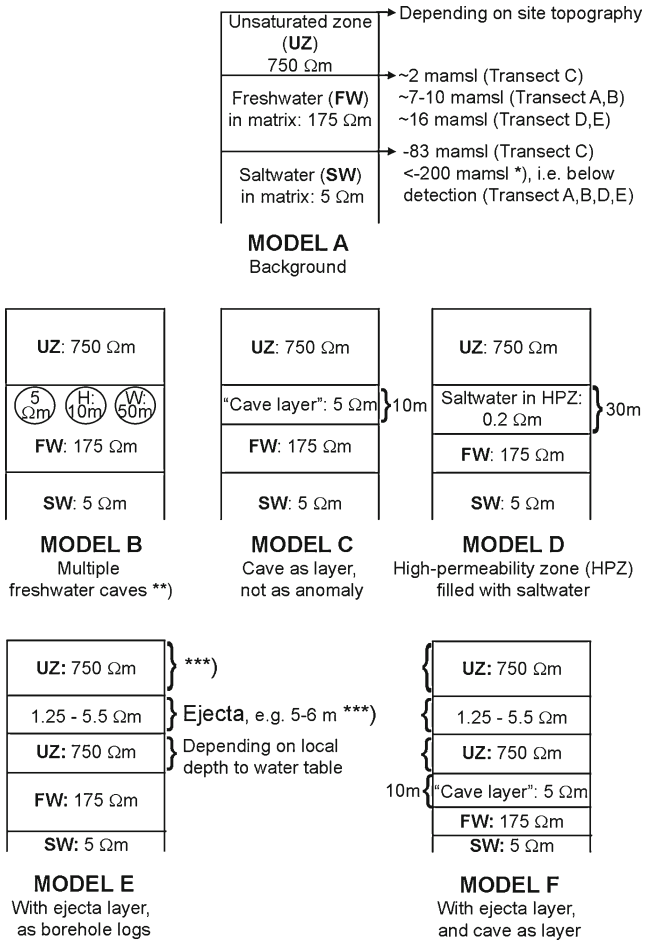

Fig. 4 Possible subsurface configurations modelled. Water levels and depths to halocline from Gondwe et al. (2010a). **)* Not measured, but estimated from the Ghyben-Herzberg relation and measured water table elevations. ***)* Realistic higher-end cave sizes from Smart et al. (2006). ****)* Estimated through fitting and comparison with nearby borehole logs. Not to scale

homogeneous halfspace of limestone saturated with saltwater. Model B represents a case where several caves are located close to each other. Realistic higher-end cave sizes from Smart et al. (2006) were used (height: 10 m; width: 50 m). Model C is a case where a cave is modeled as a layer, rather than as an anomalous body. This represents a situation in which the AEM sounding is affected by an extended, highly fractured limestone layer. The assumed thickness of the layer is 10 m—a higher-end cave height according to Smart et al. (2006). Model D has the same geometry as model C, but the cave layer is filled with saltwater instead of freshwater. Saltwater-filled caves are known in YP, but have until now only been found in the near-coastal zone. This model is thus conceptually unlikely in the inland areas. It was included in the evaluation in order to test if a hypothetical saltwater-filled fracture zone could explain the observed AEM response. A layer thickness of 30 m was assumed, which represents the upper limit of expected vertical dimensions of caves and fracture zones on the YP. Model E is a case where a low-resistivity layer is present relatively close to the ground surface, as found in borehole logs by Gondwe et al. (2010a) and interpreted as the ejecta layer. The resistivity values of this layer are taken from the borehole logs. Model F is similar to Model E, but also includes a freshwater-saturated 'cave' layer, starting at the water table, and extending 10 m down (i.e. a combination of model E and model C). In the forward calculations, water level elevations and halocline depths were taken from Gondwe et al. (2010a), surface elevations from SRTM. Ejecta thicknesses were estimated through model fitting and comparison with nearby borehole logs.

Results

This section presents the results of the regional-scale mapping using Landsat imagery and Shuttle Radar Topography Mission data and the results of the targeted AEM surveys over selected structures.

Structures identified on Landsat imagery

Structures identified on the optical satellite imagery are shown in Fig. 2a. The longest structures were located in the hilly area and in the transition zone, and a few of them extended for short distances into the flat area. In addition, some shorter structures were identified near the northern part of Sian Ka'an and one at the Holbox fracture zone. The structures in the hilly area and the transition zone were 50 km to >150 km long and transected the hilly area in a predominantly south–southwest to north—northeast direction. They were relatively densely spaced towards the lower parts of the hilly area and the transition zone and were sub-parallel here. In the area near Presidente Juarez, the structures had a braided pattern and intersected each other. Soil maps mainly indicate gleysols (undrained and/or waterlogged soils) or vertisols (soils with high content of expansive clays) in the area of the mapped structures. In some cases, e.g. near the braided patterns, the soil map indicates saline soils (INEGI 1997).

The result of the DEM-based river delineation showed some correspondence with the delineated structures, mainly in the hilly area and transition zone (Fig. 5). Only a few of the rivers delineated from the DEM are mapped as perennial or ephemeral rivers on official maps (Fig. 1). While most delineated structures corresponded with topographical depressions, some structures had no distinct expression in the elevation data. One example is shown in Fig. 6 where river-like line-shaped features appeared in Landsat imagery, but no rivers were mapped by the DEM-based river delineation routine (highlighted with arrows).

The rivers delineated from the DEM terminated before reaching Sian Ka'an. The termination point was near the 20 m topographical contour line (Fig. 5). Possibly this shift in elevation demarks an ancient coastline (Gondwe et al. 2010a), and no rivers were delineated beyond this point because of insignificant topographical relief in this area.

 DOI 10.1007/s10040-012-0877-8

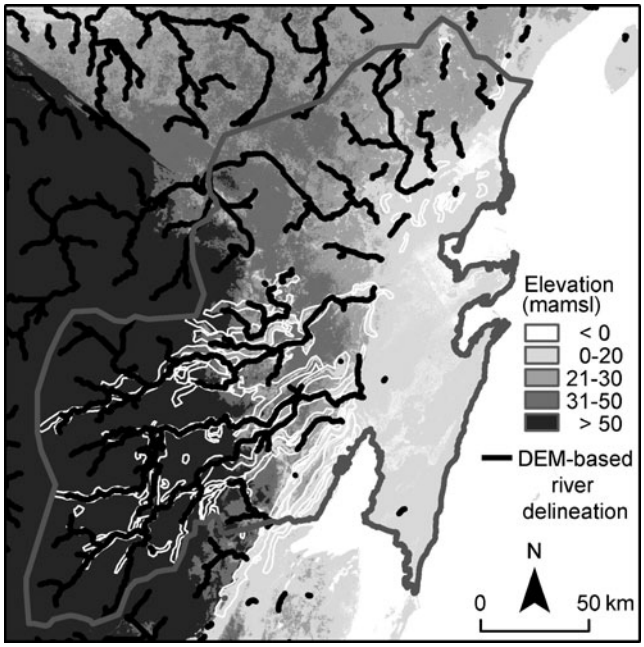

Fig. 5 Location of the rivers (*black*) automatically delineated based only on topographical relief. Topography shown as background map. The structures delineated from inspection of satellite imagery are outlined in *white*

AEM results over the Holbox fracture zone

About 1200 frequency-domain AEM line-kilometers were flown over the area of the delineated southern extension of the Holbox fracture zone, spanning an area from the Caribbean coast to 12 km inland, 10 km wide. AEM flight line spacing was generally 100 m, but only 200 m in a 2-km-wide section covering part of the fracture zone. Figure 7 presents the southern part of the Holbox fracture zone, which was outlined using SRTM elevation data, Landsat band 4 and a map of cenote (i.e. sinkhole) density. In addition the AEM results for frequencies 3200 Hz and 7190 Hz, transformed with Eq. 3, are shown. The AEM data showed markedly stronger signals over the Holbox fracture zone, as indicated in Fig. 7 with large arrows and colored polygons. The area which shows strong signals in these frequencies corresponds well with the Holbox fracture zone's southern extension (Fig. 7e). The width of the anomalous zone was about 1–2 km. Both frequencies clearly outlined the open water body Laguna La Union, and its surroundings which are not covered by open water, but are known to have high soil moisture content.

Moreover, the dataset showed four other areas of generally high signal strength. They are marked with numbered small arrows in Fig. 7 and included: (1) an area with a line of small cenotes, located in the immediate upstream extension of the Naranjal cave system; (2) the town of Tulum (likely caused by anthropogenic noise, e.g. power lines corrupting the AEM signal); (3) a flooded area at the coast; and (4) part of the Sac Actun cave system.

Layered 1D-inversions of the Holbox dataset supported the qualitative findings in the aforementioned. Areas of

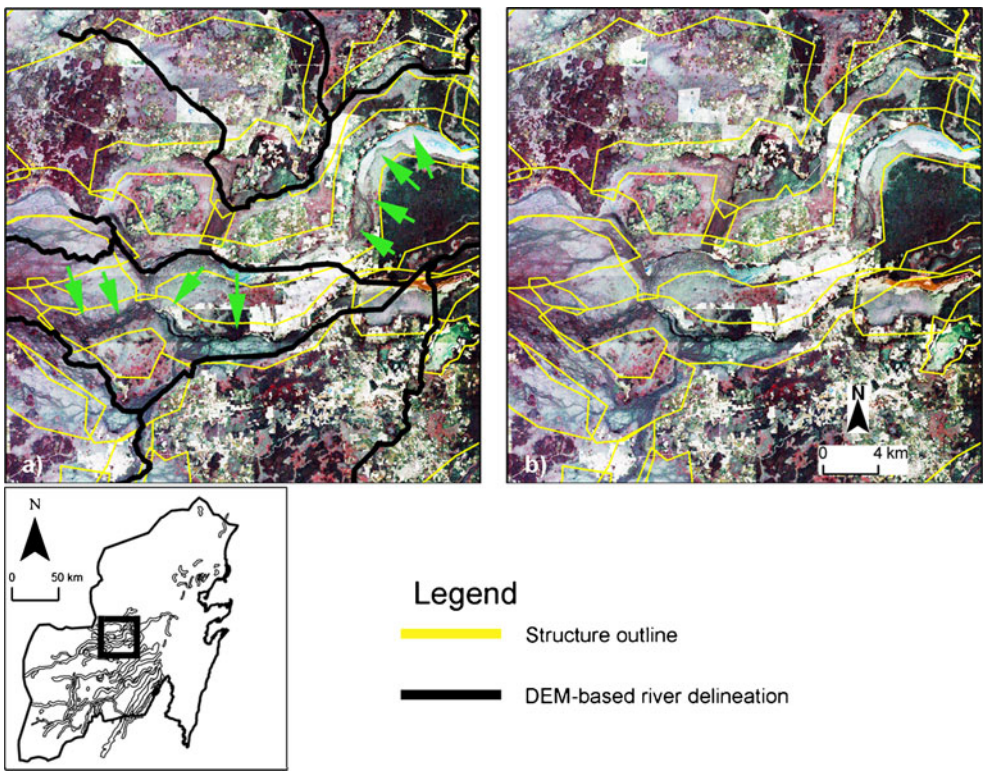

Fig. 6 Example of how, in some cases, river-like linear features can be seen in Landsat imagery but in other cases the automatic river delineation does not always put a river atop of such features (**a** highlighted with *green arrows*). In **b** the equivalent image is given without the automatically delineated rivers overlain, so the structures marked by the automatic river delineation can be seen more clearly. Background image as in Fig. 3b

 DOI 10.1007/s10040-012-0877-8

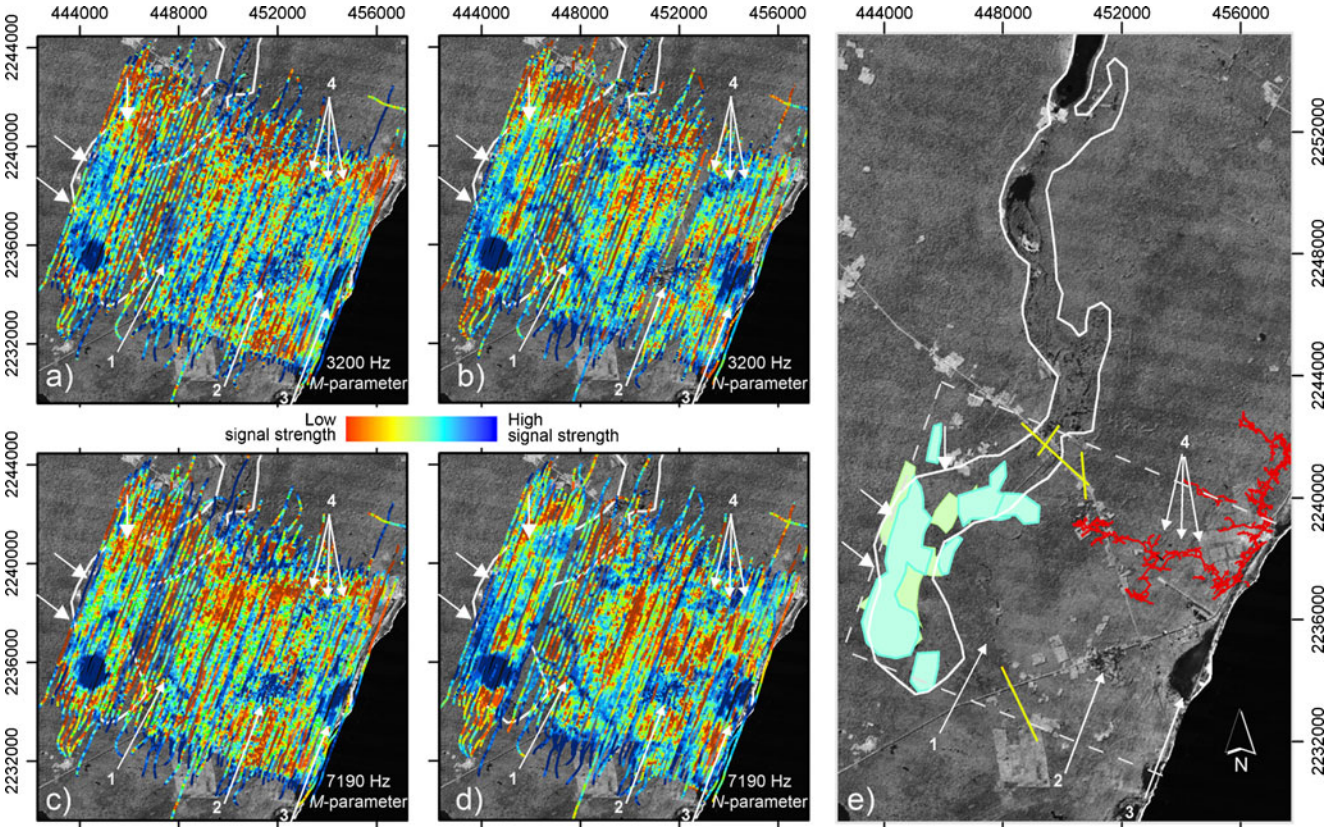

Fig. 7 **a**–**b** Response parameters *M* and *N* for the 3200 Hz signal components, and **c**–**d** for the 7190 Hz signal components over the southern end of the Holbox fracture zone. *Large arrows* highlight anomalous areas above the Holbox zone; *small numbered arrows* highlight other features mentioned in the text. **e** Holbox fracture zone outlined as described in text (*thick white line*). Anomalous areas with high signal strength in 3200 Hz inphase signal (*blue polygons*) and 7190 Hz inphase signal (*green polygons*). The location of the Sac Actun cave system (*curving red lines*) is also shown, courtesy of S. Bogaerts, K. Davidson, D. Jones, B. Phillips and R. Schmittner. Naranjal cave system and Aktun Ha and Tortuga cave systems (location coarsely indicated, *straight yellow lines*) modified from Smart et al. (2006). *Dashed grey line* outlines area surveyed with frequency-domain AEM. Background image: Landsat TriDecadal TM band 4; *dark areas* indicate high soil moisture or open water. The circular high conductivity anomaly around 2236000 mN, 444000 mE is Laguna la Union

generally lower resistivity corresponded with the location of the Holbox depression (sounding 170–510) and an agricultural field, probably irrigated (sounding 100–170; Fig. 8). In the Holbox depression, the bulk resistivity was about 50 Ωm, whereas outside the depression it was >130 Ωm. A layer of about 1–4 Ωm near –20 mamsl was mapped in good correspondence with the expected depth of the halocline. Around Laguna La Union, the zone of lower resistivity extended all the way to the surface, and was 5–15 Ωm; this value is in good correspondence with the expected resistivity of a surface freshwater body. Outside the Holbox fracture zone, inverted bulk resistivities were generally higher than 50 Ωm, except around cenotes (Fig. 8).

AEM results over the inland structures

Five transects over the mapped structures located inland were flown with AEM (transects A–E, Fig. 9). Each transect consisted of 4–6 parallel flight lines, spaced 100 m apart. The measured signals, transformed with Eq. 3, showed high signal strength anomalies over most of the structures (Fig. 9). Anomalies were especially distinct in the inphase components of frequencies 3200 Hz and 7190 Hz, but were also present in most of the other signal components. The 3200 Hz and 7190 Hz are the most suitable frequencies of the Austrian airborne system to detect cave systems in this geological environment because the skin depths associated with these frequencies coincides with the expected depths of the caves. Generally, the quadrature components of the Austrian airborne system drift more than the inphase components. The widths of the anomalous areas ranged from 1 to 5.5 km.

Spectral gamma ray measurements showed distinct anomalous composition of natural gamma radiation over structures (Fig. 10). The anomalous gamma-signal was predominantly composed of radiation from thorium and uranium, whereas the background gamma signal mainly originates from potassium. Anomalous signatures in the gamma ray measurements and in the AEM data show a strong spatial correlation (compare Fig. 9 and 10).

In 1D layered inversions, the anomalous zones were either inverted as a low-resistivity layer (1–2 Ωm) of 5-7 m thickness located at shallow (e.g. 5–8 m) depth, or as a low-resistivity layer (1–2 Ωm) extending from about 10 mbs to the bottom of the inverted space (30 mbs).

To further analyze the measured AEM signals, the AEM responses over synthetic subsurface resistivity

 DOI 10.1007/s10040-012-0877-8

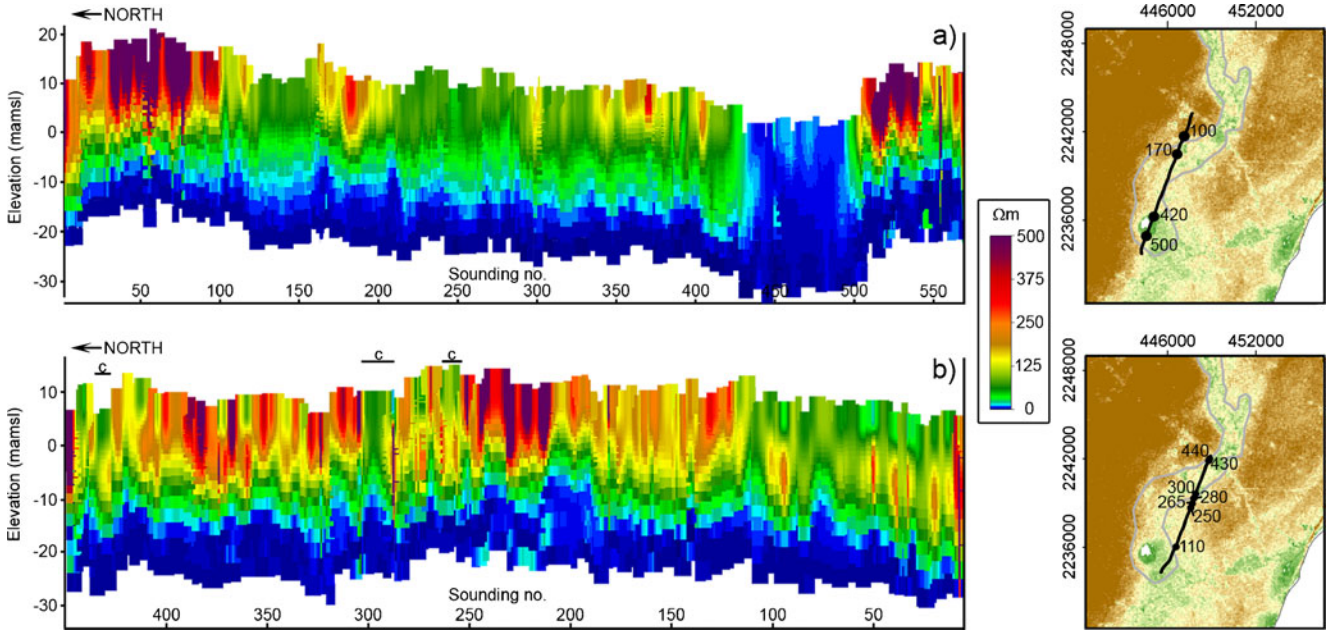

Fig. 8 Inversion results from profiles over the Holbox fracture zone. **a** Soundings 170 to ~500 are within the delinated Holbox zone and appear as more highly conductive than surroundings. Sounding 100–170 likely represents an irrigated field. **b** The line only crosses a higher conductive part of the Holbox zone at sounding 0 to ~110. The *c* symbols indicate location of known cenotes. Location maps at *right side* show topographic relief from SRTM (*brown*: elevations>20 mamsl, *green*: elevations<0 mamsl. *Numbers* are the sounding numbers of each profile. The conductive feature at sounding number ~430 –500 in Laguna La Union (**a**)

models were computed. Possible subsurface configurations are presented in Fig. 4. Sensor elevations were taken from the field dataset. The simulated signal over model A was much lower than the measured data (Fig. 11). Including multiple large freshwater-filled caves next to each other (model B) could not bring the signal up to measured levels. These caves, although large, only increased the AEM signal by 10–15 ppm compared to model A (Fig. 11). Furthermore, simulated anomalies over caves were much narrower (only ~150 m wide) than the measured anomalies. Modelling a freshwater cave as a full layer instead of separate individual caves (model C), or using the conceptually unlikely model D of saltwater in a high permeable zone, also did not result in satisfactory correspondence between measured and observed signals (examples shown in Fig. 11). Hence, the AEM anomalies in the inland areas are most likely not caused by caves or high-permeable zones. Instead, a proposed ejecta-layer (model E) was simulated. This gave a good fit to the measured data (examples shown in Figs. 11, 12 and 13), except for the 28850 Hz inphase and the 340 Hz quadrature components, for which the simulated data are often higher than the measured data (Figs. 11c, 12c and e, 13c).

Examples of how model E fits to the data are shown in Fig. 11, 12 and 13 for the transects A, B and D. Transect C and E are similar to transects B and D, respectively, and are therefore not shown for the sake of brevity. In the following, the subsurface models recovered from the AEM surveys for the various transects are discussed in detail and are compared with borehole log data obtained from boreholes located close to the transects.

Transect A was located in the lower transition zone, with elevations between 20 and 35 mamsl. In a borehole log located 1 km from the AEM transect, the ejecta layer has been detected at elevations of 5–13 mamsl, with a resistivity of about 5 Ωm (Fig. 11e and f; Gondwe et al. 2010a). The AEM signal measured over transect A corresponded well with an ejecta layer of 5 Ωm, located at approximately 7 to 13 mamsl, i.e. a model E subsurface configuration. Moderate variability in the thickness of the ejecta layer or its resistivity could explain variations in measured anomaly strength.

Transect B was located in the transition zone at elevations between 30 and 40 mamsl. The most western end transected a part of the hilly area (elevations >50 mamsl). The ejecta layer has been found in borehole logs located 2 km (Nuevo Israel), 3 km (Las Panteras), 6 km (Emiliano Zapata) and 7 km (Presidente Juarez, only gamma log) from the transect (Gondwe et al. 2010a; Fig. 12). The measured AEM signals could be reproduced assuming the subsurface resistivity model E with an ejecta layer of about 1.25 Ωm, located at approximately 15–20 mamsl. In the hilly portion of transect B, the layer needed to be located much higher, around 60 mamsl, to match the measured AEM signal.

Transect C, also located in the transition zone at elevations between 30 and 40 mamsl, could be modeled with a similar subsurface configuration as transect B, i.e. with an ejecta layer around 15–20 mamsl (model E), and in some cases an additional a low-resistive layer at depth (model F).

Transects D and E were located in the hilly area (elevations >50 mamsl). Figure 13 gives an example of model fits to transect D. An ejecta layer of about 3 Ωm located at shallow (<12 m) depth, but varying elevation

 DOI 10.1007/s10040-012-0877-8

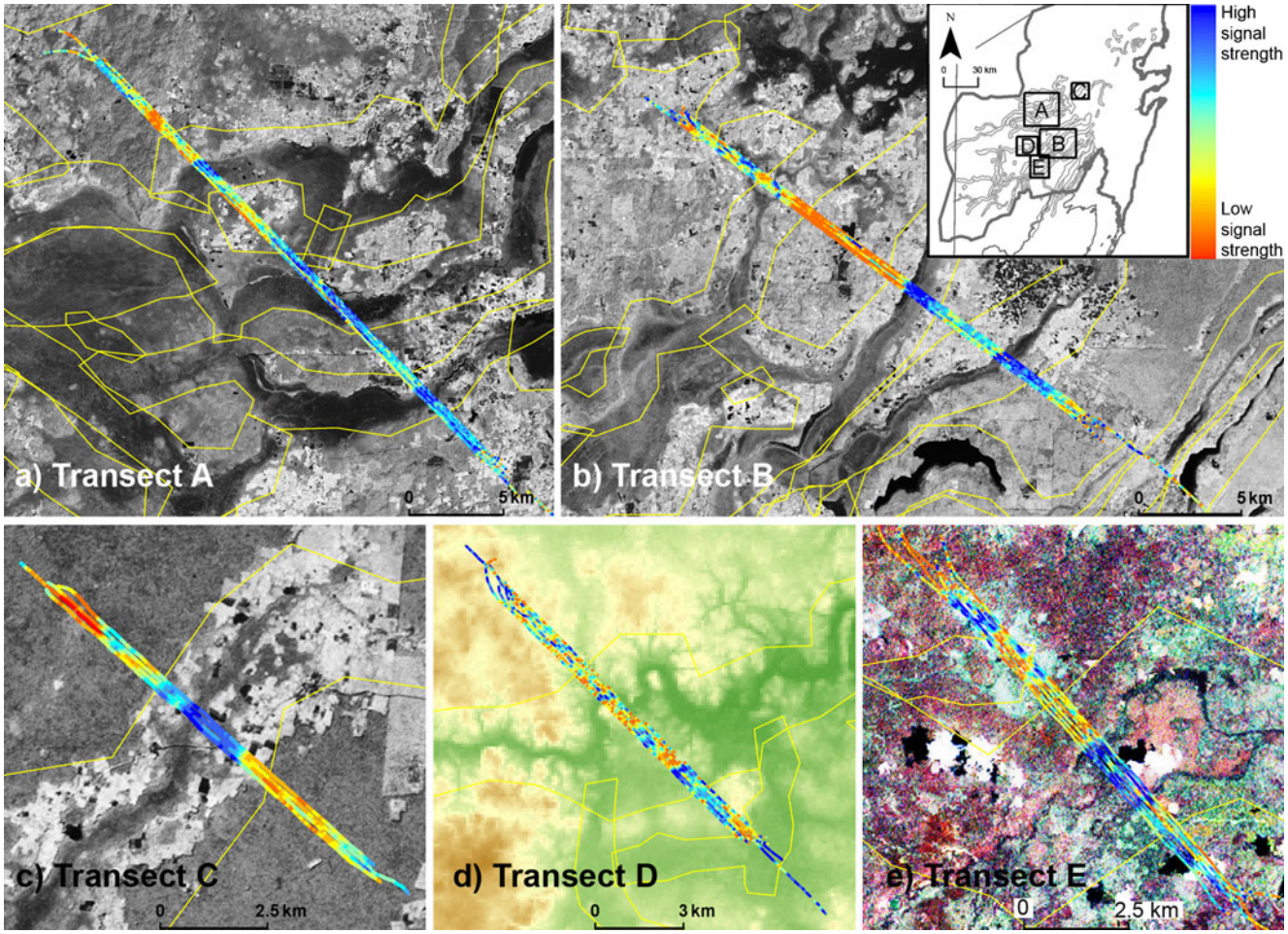

Fig. 9 Frequency-domain AEM signal measured over inland structures, transformed with Eq. 1. 7190 Hz*M* parameter (**a**,**b**,**c**,**e**) and 3200 Hz*M* parameter (**d**). *Thin yellow lines* outline structures. Landsat TriDecadal TM band 4 (background of **a**–**c**); SRTM topograph, *brown* is high elevation, *dark green* is low elevation (background of **d**); Landsat ETM+, RGB: band 2, band 3, band 1 (background of **e**)

(50–100 mamsl; model E), could explain the measured signal well, and corresponds to borehole logging results 4 km from the transect (Fig. 13). In a ~ 7-km-wide band around the small river crossing the transect, a deeper low-resistive layer (5 Ωm; model F) was required in order to match measured AEM signals.

Discussion

This section discusses the specific geological and hydrogeological findings for the Holbox fracture zone and the inland structures. Subsequently, the hydrological significance of the mapped structures is discussed, both in terms of surface and subsurface hydrology. The section concludes with a discussion of the potential of the presented multi-scale mapping approach both for the YP and beyond.

The southern extension of the Holbox is a high-permeability zone

The AEM results indicate that the Holbox zone's proposed southern extension has a lower resistivity than its surroundings. Assuming fully saturated conditions and typical values (a=1.5, m=2) for the constants in Archie's Law (Eq. 2) and assuming a freshwater resistivity (ρ_w) between 4 and 10 Ωm (Beddows 2004), the bulk resistivities found in the inversion of the AEM data indicate that the porosity inside the Holbox zone is 0.41 ± 0.13, while outside the Holbox zone, the porosity is 0.25 ± 0.1. The uncertainty bounds on the porosity estimates were computed using error propagation assuming an uncertainty of 20 % for all the inputs into Eq. 2. Due to the high uncertainties associated with the parameterization and applicability of Archie's law in this geological environment, the porosity difference between the Holbox structure and its surroundings is not significant. However, the results suggest a higher porosity inside the Holbox fracture, which could be related to fracturing. Interestingly, the southern extension of the Holbox fracture zone is aligned with large lakes in the area (Laguna La Union, Laguna Ka'an Luum, Laguna Nopalito, Laguna Chunyaché), and with the fault suggested by Gondwe et al. (2010b). The resistivity values of the freshwater-saturated bulk matrix outside and inside the Holbox zone correspond well with values reported in Supper et al. (2009).

 DOI 10.1007/s10040-012-0877-8

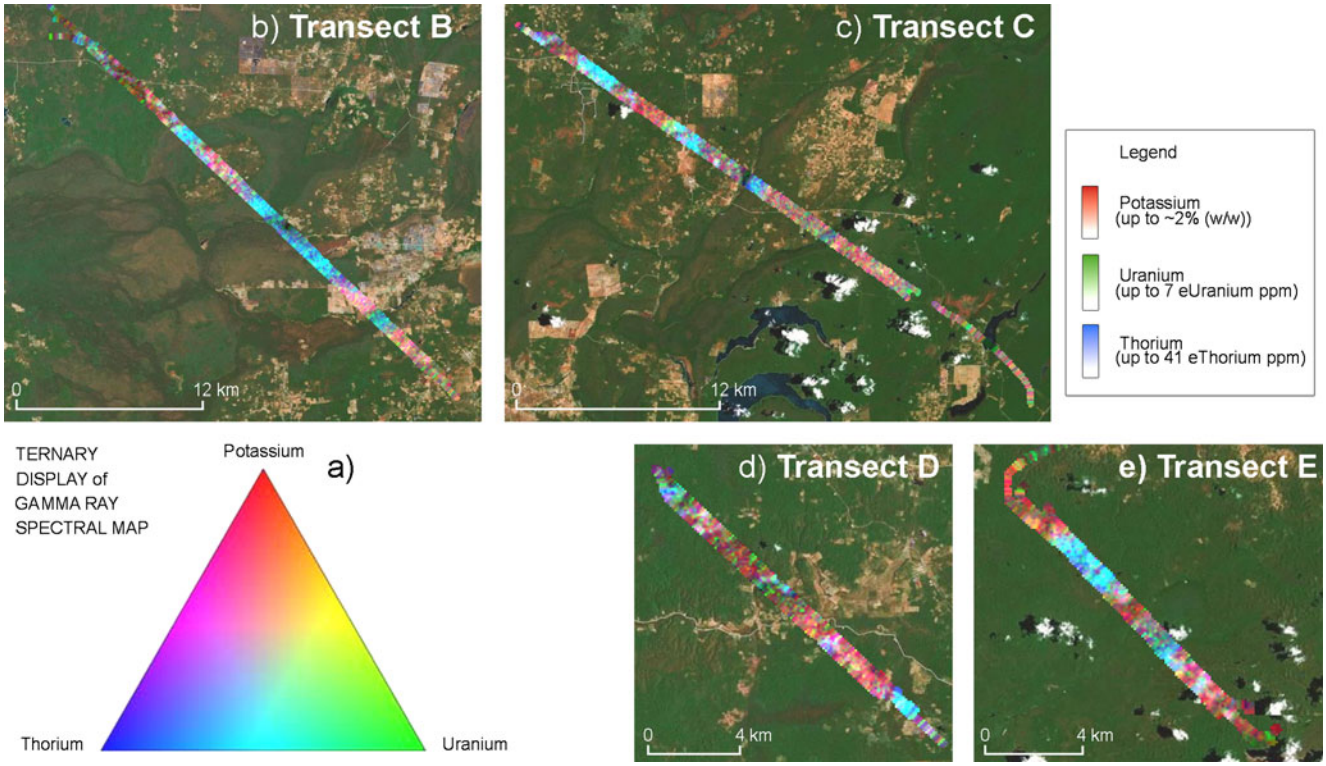

Fig. 10 Spectral gamma-ray across **b** transect B, **c** transect C, **d** transect D and **e** transect E, displayed as *red-green-blue* ternary ratio. **a** shows how to interpret the colors

Two cave systems, Aktun Ha and Tortuga, which are located in the zone, further support the generally high permeability of this area (see cave maps in Smart et al. 2006). Dye tracing in Aktun Ha (Beddows and Hendrickson 2008) and regional-scale hydrological modelling (Gondwe et al. 2011) indicate south–north-directed flow within the Holbox zone.

The Holbox dataset also confirms that caves can be mapped with AEM in the study area, as the Sac Actun cave system is clearly seen (Fig. 7). This application was first demonstrated by Supper et al. (2009).

Interpretation of structures located inland

The structures delineated near the Bay of Chetumal (e.g. the Laguna de Bacalar depression) are known to be part of the Río Hondo fault system. The other inland structures in the lower part of the hilly area and in the transition zone are also likely related to this fault system, given their proximity and sub-parallel nature. The "S"-shape appearing in the transition zone on many of the mapped structures is characteristic of *en echelon* faults, and supports the association between the structures and faults. *En echelon* faults in the study area were described by Lara (1993).

The inland structures showed high AEM signal anomalies, just as the Holbox fracture zone did. However, the nature of the anomalies was different. Likely, the anomalies measured over the inland structures are caused by a 5–6 m thick layer of low-resistivity material (1–5 Ωm), located at relatively shallow depths (the model E case). The data fit achieved with this model is good. Especially the 3200 Hz and the 7190 Hz components fit well, but modeled signals are sometimes higher than measured in the 340 Hz and the 28850 Hz components. Other subsurface resistivity models can therefore not be ruled out based on the AEM results. However, model E is consistent with borehole logs and measured halocline depths.

The low-resistive ~5-m-thick layer was interpreted by Gondwe et al. (2010a) as ejecta. The AEM interpretation indicates that the layer is located at approximately the same depths, but variable elevations, throughout the hilly area, while it is located at constant elevation in the transition zone, with a slight tendency of being buried deeper at locations further away from the hilly area. The borehole logging and ground-based transient electromagnetic measurements from the area (Gondwe et al. 2010a) support this finding. One possible explanation is that at the time of the Chicxulub impact, only the hilly area was exposed at the land surface, while the flat area was covered by the ocean. The steep drop in elevation between the hilly area and the transition zone, of more than 10 m (from 50 to <40 mamsl) in less than a km, suggests the presence of the ancient coastline here. The late Cretaceous land surface was heavily karstified (Dillon and Vedder 1973; Pope et al. 2005), with an undulating relief, while the ocean floor was comparably flat. The ejecta blanket was deposited on top of the Cretaceous surface; both on the land surface (hilly area) and in the shallow ocean (transition zone and flat area). This is a possible explanation for the fact that the anomalous layer is found

 DOI 10.1007/s10040-012-0877-8

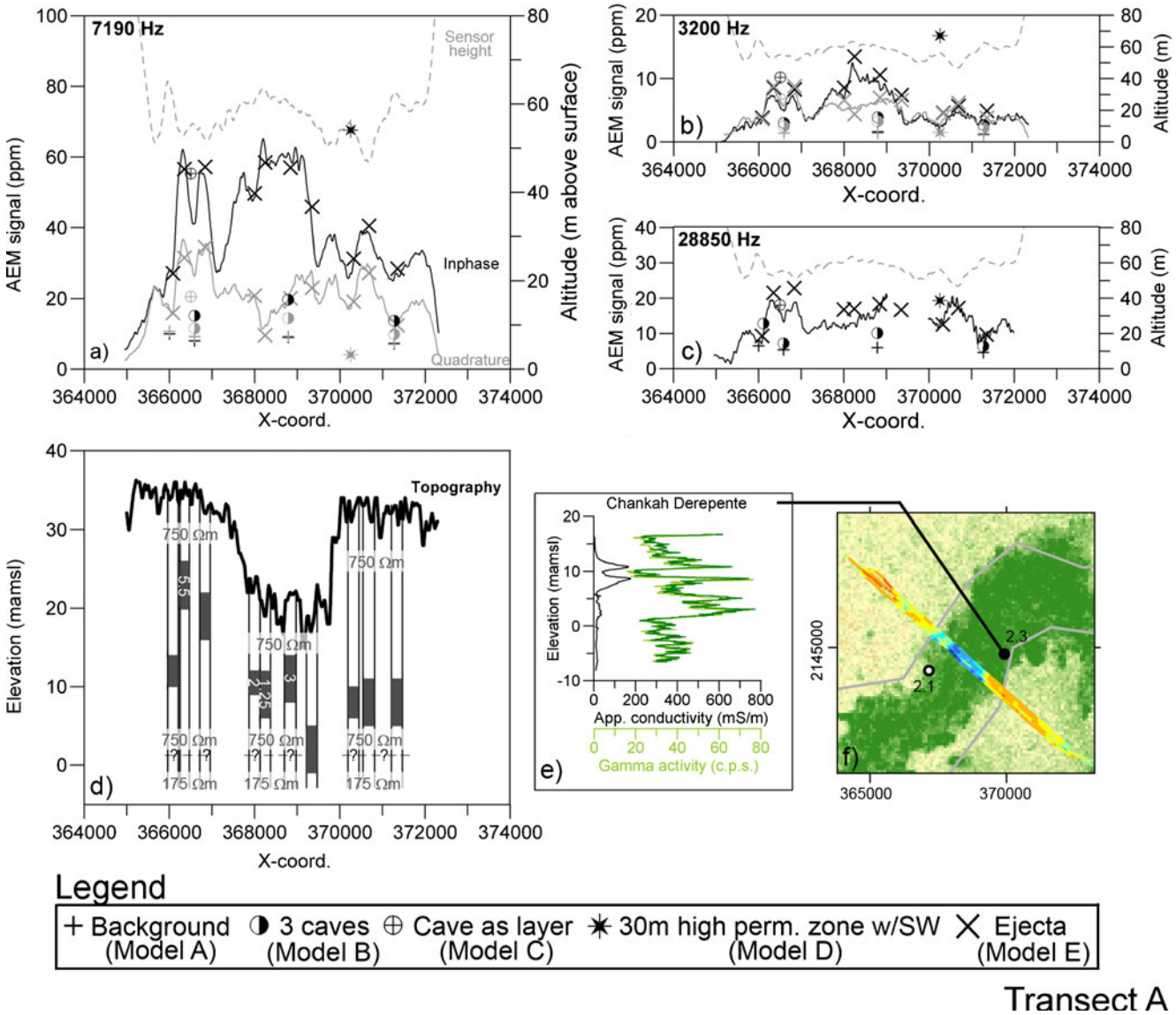

Fig. 11 **a**–**c** AEM data (*lines*) from a flight line in transect A, along with forward modelled signals (*symbols*). **d** Topographic relief of the transect and earth models corresponding to x-symbols (see **a**). **e** Nearest borehole log, from Gondwe et al. (2010a). **f** Location map, displayed on topographic background (*dark green* is lower elevation). AEM data legend as in Fig. 9. *Black dot*: Location of logged borehole. *White dot* indicates where water level was measured. *Numbers* indicate measured water levels in mamsl from Gondwe et al. (2010a)

at similar elevations in the flat area and transition zones, but at varying elevations in the hilly area.

Ejecta has been found in 200–400 m thick sequences in wells near the impact crater (Rebolledo-Vieyra et al. 2000; Urrutia-Fucugauchi et al. 1996; 2004; 2008), but elsewhere thinner sequences have been found. Urrutia-Fucugauchi et al. (2008) suggested significant erosion of the ejecta blanket following the finding of a ~34-m-thick ejecta unit near Valladolid, and Pope et al. (2005) found Cenozoic sediments atop a *weathered* ejecta surface at one site. Following the ejecta deposition, erosion may therefore have taken place, reducing the thickness of the ejecta layer to the thicknesses mapped in this study and in Gondwe et al. (2010a). Reported ejecta thicknesses in southern Quintana Roo vary from the 3–8 m seen in most borehole logs (Gondwe et al. 2010a) and observed in outcrops by Pope et al. (2005; 4–8 m, bases not always observed) to 15 m (Reforma-log, Gondwe et al. 2010a) and 16 m (Albion Island, Ocampo et al. 1996), supporting the idea of erosion of the blanket after deposition. Subsequently, Cenozoic sediments would have been deposited atop the ejecta in the areas covered by water—which is in good correspondence with the present geologic map (Fig. 1).

The inland structures likely produce AEM anomalies because the Miocene–Pliocene sediment layer on top of the ejecta layer is thinner here than in the surrounding terrain. At constant flight height above terrain, the low-resistivity ejecta layer is thus located closer to the AEM sensor over the structures, giving a higher measured signal (e.g. Fig. 11d). A possible process causing reduced sediment thickness and topographic depressions is fluvial erosion. The structures in the transition zone are mostly aligned with the preferential

 DOI 10.1007/s10040-012-0877-8

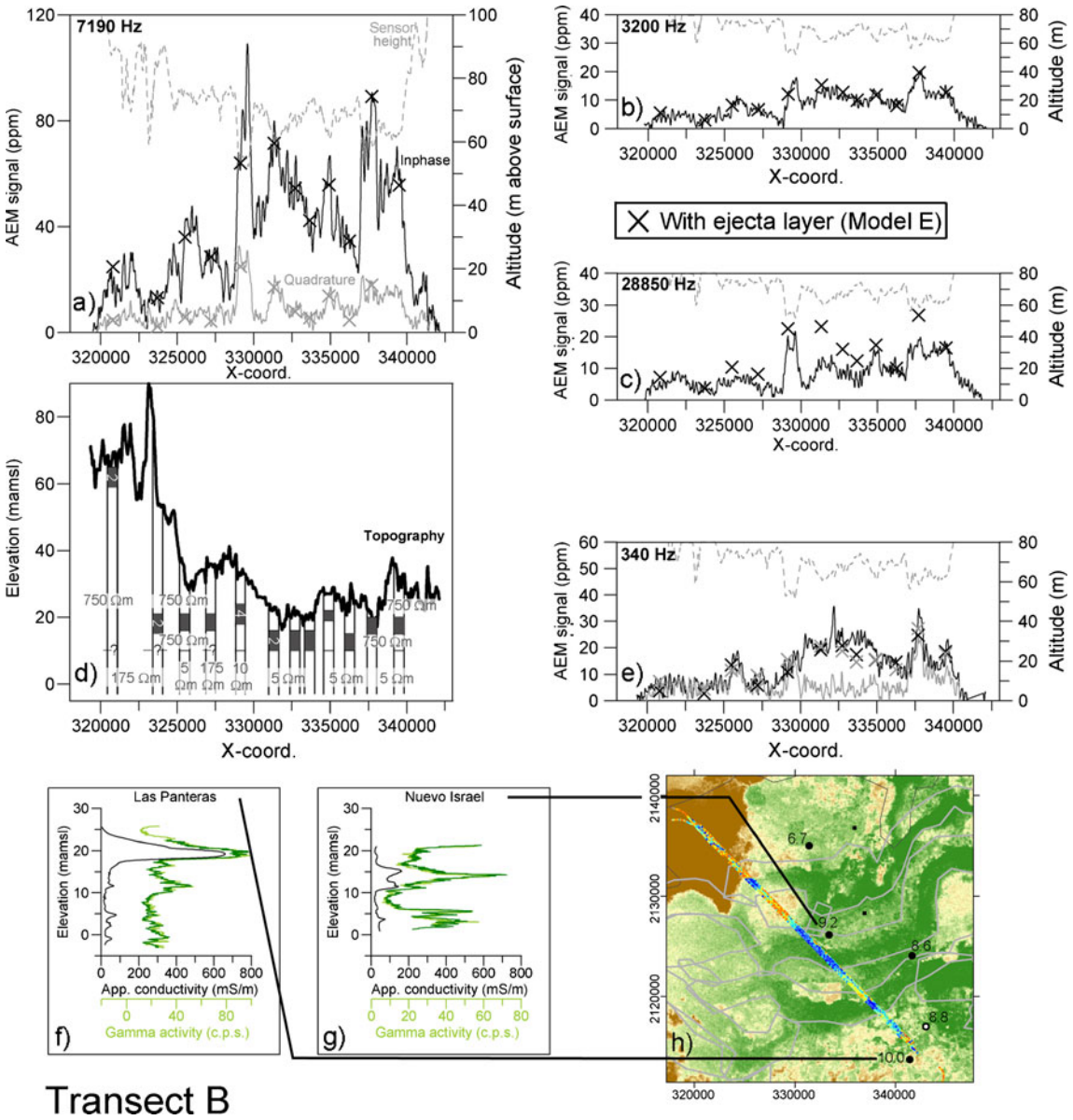

Fig. 12 **a**–**c** and **e** AEM data (*lines*) from a flight line in transect B, along with forward modelled signals (*symbols*). **d** Topographic relief of the transect and earth models corresponding to x-symbols (see **a**). **f**–**g** Nearest borehole log, from Gondwe et al. (2010a). **h** Location map, displayed on topographic background (*dark green* is lower elevation, *brown* is higher elevation). AEM data legend as in Fig. 9. *Black dot* is the location of logged boreholes. *White dot* shows where water level was measured. *Numbers* indicate measured water levels in mamsl from Gondwe et al. (2010a). *Small black squares* are wells with perched water encountered, levels not shown (from Gondwe et al. 2010a)

surface water flow paths in the hilly area delineated from the DEM, which supports this hypothesis. Possibly, surface runoff collected in slight depressions or rifts forming over the Río Hondo faults, which were still active in the Cenozoic (Dillon and Vedder 1973).

The anomalous spectral-gamma ray signal may also be related to the ejecta. Anomalously low potassium radiation relative to thorium and uranium radiation has been reported for ejecta from the Cretaceous/Paleogene boundary layer (Paulsen and Lind 1997). Since the measured spectral-gamma ray signal originates from the first ~35 cm of the soil, the anomalous gamma signal observed over the structures cannot be caused by a buried ejecta layer at ≥5 mbs. However, the ejecta layer is exposed to erosion in the hilly area. Erosion of ejecta material in the hilly area and subsequent deposition of the same material in the structures, e.g. through seasonal surface-water runoff in the structures, could possibly explain the anomalous gamma signal over the structures. Alternatively, the measured gamma-signals may simply be caused by a different soil type in these seasonally waterlogged areas. The available data do not support a final conclusion on this question.

The 340 Hz AEM signal showed high anomalies over some mapped structures—anomalies which were not matched by modeling the ejecta layer (model E) alone. An example is seen in Fig. 12e at coordinate x=326000 and between x-coordinates 327500 and 340000. These anomalies could be reproduced with an additional low-

 DOI 10.1007/s10040-012-0877-8

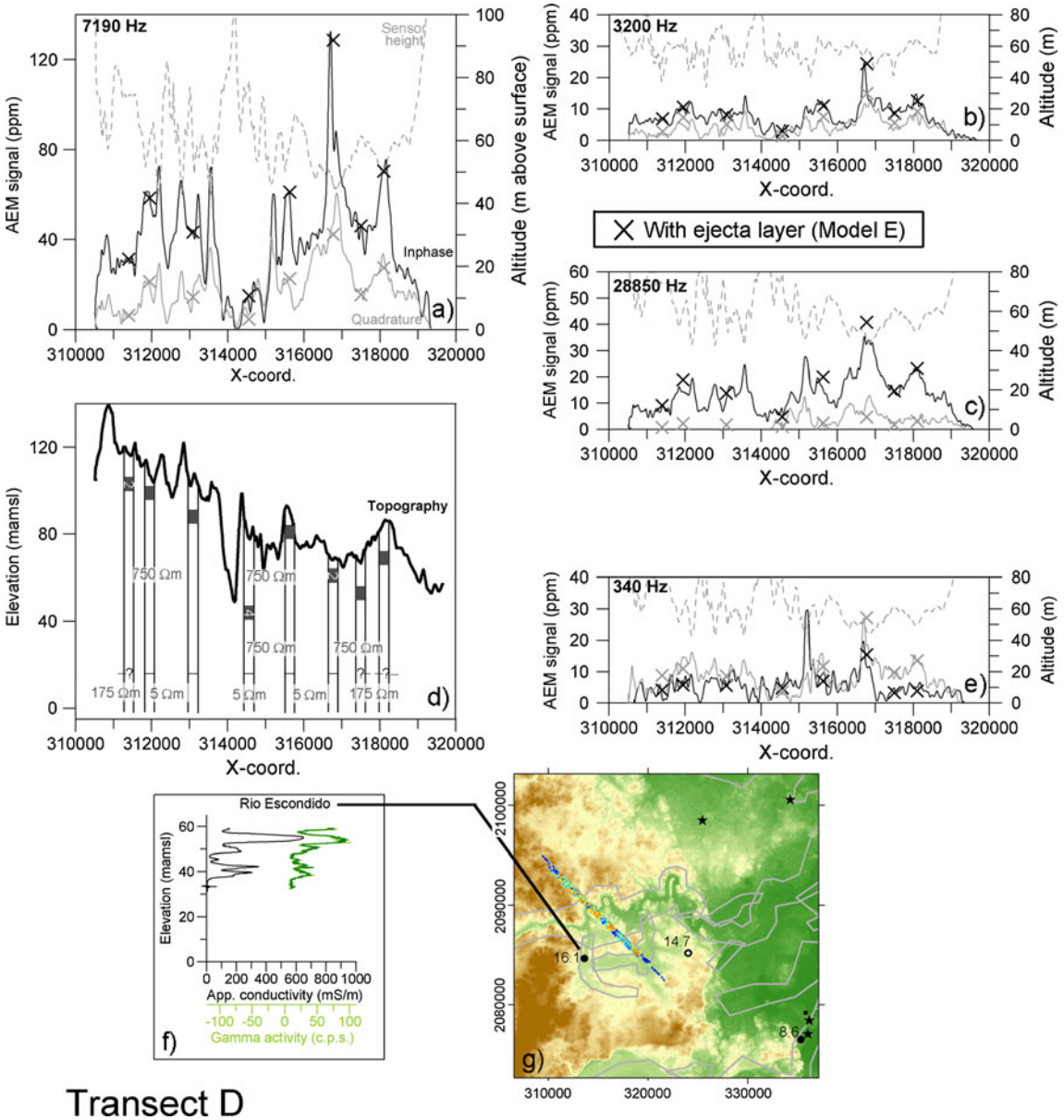

Fig. 13 **a**–**c** and **e** AEM data (*lines*) from a flight line in transect D, along with forward modelled signals (*symbols*). **d** Topographic relief of the transect and earth models corresponding to x-symbols (see **a**). **f** Nearest borehole log, from Gondwe et al. (2010a). **g** Location map, displayed on topographic background (*dark green* is lower elevation, *brown* is higher elevation). AEM data legend as in Fig. 9. *Black dot* is the location of logged boreholes. *White dot* shows where water level was measured. *Numbers* indicate measured water levels in mamsl from Gondwe et al. (2010a). *Small black squares* are wells with perched water encountered, levels not shown (from Gondwe et al., 2010a). *Black stars* are sites with ejecta according to Schönian et al. (2004) and Kenkmann and Schönian (2006)

resistivity zone of ~5 Ωm located below the ejecta layer, starting at the water table (model F). This may indicate that the delineated structures are spatially correlated with zones of higher matrix porosity, i.e. preferential flow paths. However, the quality and coverage of the available AEM data does not support a robust conclusion on this issue.

Relevance of the regional-scale structures for surface water hydrology

The delineated structures collect surface runoff due to their relatively low topographic elevation and possibly due to low-permeability soil cover. This is corroborated by the fact that swamps, poljes, ephemeral streams, waterlogged soil types and the few lakes existing on the YP are associated with the delineated structures. The role of poljes and bajos in the regional hydrology, has not previously been described in the existing literature on the Yucatecan inland swamps (e.g. Pope and Dahlin 1989; Gunn et al. 2002; Tun-Dzul et al. 2008; Beach et al. 2008). Runoff is observed in many structures during parts of the year, as evidenced by culverts and bridges built across them.

Poljes and flat-bottomed valleys can also be identified on official geologic maps and the DEM in Campeche's

 DOI 10.1007/s10040-012-0877-8

hilly regions on the western YP. However, in Campeche, only the flat-bottomed polje-features are seen. In Quintana Roo, the structures are more incised, due to their possible formation in association with the Río Hondo fault system. Spectral anomalies in Landsat Band 4 are only observed for the incised structures and not for the flat-bottomed poljes in Campeche and in the hilly parts of the study area (Morocoy and Nuevo Becak poljes). It is interesting to note how the incised structures of the study area seem to point towards Sian Ka'an–the only extensive wetland on the peninsula.

Relevance of the regional-scale structures for groundwater flow

Due to the shielding effect of the ejecta-layer, AEM surveys over the inland structures cannot unambiguously determine their subsurface expression. However, faults elsewhere in the study area are associated with high permeable zones. Apart from the Holbox zone, also the fault in which Laguna de Bacalar is located, is associated with underground water circulation through a connected karst system (Gischler et al. 2008). This lake has the same width as most of the delineated structures (1–2 km). It is up to 15 m deep, and hosts up to 90-m-deep freshwater-filled cenotes (Gischler et al. 2008). Karstic caves are generally known to often form along faults and fracture systems (Ford and Williams 2007). In the study area, breakdown-features near Ocom (at approximately 19.5° N/88.1° W; NUTM16 (WGS84) 38400 mE, 2152700 mN), on one of the delineated structures, form seven lakes 'on-a-string', known to be fed by submerged sinkholes. In the hilly area, some sinking streams (ponors, e.g. Río Escondido), have been observed. The streams flow into sinkholes and disappear from the land surface. In neighboring Belize, poljes are associated with ponors and underground caves (Miller 1996). All these attributes suggest the possibility that the structures may be underlain by high-permeable zones.

Further indications on the hydrogeological properties of the structures can be obtained from inverse groundwater modeling. Multiple model simulation (Refsgaard et al. 2006) was used to compare hydrologic models of the area with or without assigning a hydraulic conductivity contrast between the structures and the background (Gondwe et al. 2011). Automatic calibration (inverse optimization) of hydraulic conductivities using measured heads from 59 groundwater wells yielded a hydraulic conductivity of the structures which was one to two orders of magnitude higher than the hydraulic conductivity of the background. Simulated flows in these structures had the same order of magnitude as those measured in Quintana Roo conduits (Gondwe et al. 2011). However, Gondwe et al. (2011) showed that equally good fits to heads could be achieved with a uniform hydraulic conductivity and a variable coastal flow resistance. The nature of the structures must therefore be investigated further in order to conclusively determine their hydrogeological properties.

Potential of the multi-scale mapping approach for the YP and beyond

Although it has been demonstrated that frequency-domain AEM can detect caves and larger-scale high permeability zones, the performance of the method depends strongly on the local geological conditions. Forward modeling shows that the sensitivity of the AEM surveys is insufficient to detect high porosity zones located below an ejecta layer (e.g. 5–10 mbs, 1–5 Ωm).

When no low-resistivity layer is present, the ability of frequency-domain AEM to detect high permeability zones, including caves, is not fully understood. Forward modelling of the Ox Bel Ha signal measured by Supper et al. (2009) shows that using known cave dimensions cannot bring the modelled anomaly up to the measured level (Ottowitz 2009). Possibly, the matrix surrounding the caves has an increased porosity, resulting in a low resistivity 'halo' around the actual cave, and increasing the magnitude of the anomaly. This topic has received very little attention in the literature. The limestone medium surrounding karst conduits has in one case been described as inhomogeneous, based on geophysical measurements (Guérin et al. 2009). A higher porosity surrounding cave conduits may also correspond to the proposed "annex-to-drain" conceptualization, where storage in the karst aquifer is believed to take place in large karstic voids connected to conduits (Mangin 1974; Bakalowicz 2005). In addition to the hypothetical 'halo' around caves, the frequency-domain AEM signal amplitude is particularly sensitive to the following cave parameters: the proportion of saltwater in the cave (for instance, the Ox Bel Ha caves are filled partly with fresh, partly with saline water); the size of the cave; the presence of several caves in the vicinity of each other; the shape and depth of the cave; the resistivity contrast in the geology; and the sensor height.

The multi-scale approach used for karst hydrogeologic investigation in this study can be used to focus costly and time-consuming AEM measurements over a large study area, by utilizing spectral and topographical anomalies in remotely sensed imagery and DEMs. The approach can detect karstic caves and high-permeable fracture zones under a range of geological conditions. However, the method is highly dependent on the local geology. For instance, shallow low-resistive features may shield underlying caves (e.g. compare models E and F). The YP karst aquifer is important, large and practically unexplored. The south-eastern part of the YP is geomorphologicaly different from the rest and therefore an interesting exploration target. The YP karst aquifer can be used as a test bed for karst exploration methods because of its size, low anthropogenic noise, and its layered (quasi-2D) geometry.

Conclusions

Remote-sensing data combined with DEM analysis and AEM measurements can be used to map regional-scale

 DOI 10.1007/s10040-012-0877-8

karst aquifer structure. Remote sensing can be used to delineate regional-scale structures, and to link local-scale AEM results to the catchment scale. Remote sensing and DEM analysis can guide AEM exploration when total coverage by AEM measurements is not feasible due to the size of the groundwater capture zone. The method of combining local-scale AEM measurements with regional-scale remote-sensing data analysis is applicable for analysis of other large and unexplored karst catchments as well.

The ability of frequency-domain AEM to detect underwater caves is not fully understood but depends partly on the resistivity contrast between the high-permeability zone and bulk rock matrix, the size of the anomalous zone and the proportion of saline water in the cave. Further studies are required to determine the nature of the rock matrix immediately surrounding a high-permeability zone, as this zone may have an important influence on the measured EM signals.

The delineated structures in the Sian Ka'an capture zone are possible pathways for rapid groundwater flow to the wetland, and for seasonal surface-water flow. Regional-scale karst structures are thus of great importance for the protection of well fields and groundwater-dependent ecosystems.

In the inland parts of the study area, the AEM measurements indicate the presence of a low-resistivity layer, with a resistivity of 1–5 Ωm and a thickness of 5–6 m, deposited near the surface. This layer is proposed to be ejecta from the Chicxulub impact (Cretaceous/Paleogene boundary).

Acknowledgements Financial support from the Austrian Science Fund (project L524-N10 'XPLORE'), The Nature Conservancy, UNESCO, Geological Survey of Austria, the COWI Foundation, WWF Verdensnaturfonden/Aase & Ejnar Danielsens Fond 2006 and 2007, ETH Zürich, and Technical University of Denmark is gratefully acknowledged. We thank S. Bogaerts, K. Davidson, D. Jones, B. Phillips and R. Schmittner for permission to use the Sac Actun cave map. Andreas Ahl carried out the AEM data leveling and processing prior to the data analysis and inversion presented herein.

References

Archie GE (1942) The electrical resistivity log as an aid in determining some reservoir characteristics. T Am Inst Mineral Metall Petrol Eng 146:54–62

Atkinson TC (1977) Diffuse flow and conduit flow in limestone terrain in the Mendip Hills, Somerset (Great Britain). J Hydrol 35:93–110

Avdeev DB (2005) Three-dimensional electromagnetic modeling and inversion from theory to application. Surv Geophys 26:767–799

Bakalowicz M (2005) Karst groundwater: a challenge for new resources. Hydrogeol J 13:148–160. doi:10.1007/s10040-004-0402-9

Bauer-Gottwein P, Gondwe BRN, Charvet G, Marín LE, Rebolledo-Vieyra M, Merediz-Alonso G (2011) Review: The Yucatán Peninsula karst aquifer, Mexico. Hydrogeol J. doi:10.1007/s10040-010-0699-5

Beach T, Luzzadder-Beach S, Dunning N, Cook D (2008) Human and natural impacts on fluvial and karst depressions of the Maya Lowlands. Geomorphol 101:308–331. doi:10.1016/j.geomorph.2008.05.019

Beddows PA (2004) Groundwater hydrology of a coastal conduit carbonate aquifer: Caribbean coast of the Yucatan Peninsula, México. PhD Thesis, Univ of Bristol, UK

Beddows PA, Hendrickson MR (2008) When the survey is not enough: temperature, salinity, and dye tracing reveal flow paths. In: Elliot WR (ed) Proc. 2007 Natl Cave and Karst Manage Symp, St. Louis, MO, USA, pp 198–203

Benson RC, Yuhr L (1993) Spatial sampling considerations and their applications to characterizing fractured rock and karst systems. Environ Geol 22:296–307

Bosch F, Müller I (2005) Improved karst exploration by VLF-EM gradient surveys: comparison with other geophysical methods. Near Surf Geophys 3:299–310

Cornaton F, Perrochet P (2002) Analytical 1D dual-porosity equivalent solutions to 3D discrete single-continuum models: application to karstic spring hydrgraph modelling. J Hydrol 262:165–176

Degirmenci M, Günay G (1992) Analysis of hydrologic relations between Egirdir-Beysehir-Sugla lakes system and adjacent basins by means of remote sensing techniques (southern Turkey). Environ Geol Water Sci 19(1):41–45

Dillon WP, Vedder JG (1973) Structure and development of the continental margin of British Honduras. Geol Soc Am Bull 84:2713–2732

Doll WE, Nyquist JE, Beard LP, Gamey TJ (2000) Airborne geophysical surveying for hazardous waste site characterization on the Oak Ridge Reservation, Tennessee. Geophysics 65 (5):1372–1387

Doolittle J, Collins M (1998) A comparison of EM and GPR methods in areas of karst. Geoderma 85:83–102

Ford DC, Williams P (2007) Karst hydrogeology and geomorphology. Wiley, Chichester, UK, 576 pp

Fouke BW, Zerkle AL, Alvarez W, Pope KO, Ocampo AC, Wachtman RJ, Grajales Nishimura JM, Claeys P, Fischer AG (2002) Cathodoluminescence petrography and isotope geochemistry of KT impact ejecta deposited 360km from the Chicxulub crater, at Albion Island, Belize. Sedimentology 49:117–138

Gamey TJ, Thompson M, Mandell W, Frano G (2001) Karst pathway delineation using combined spatial and geophysical analysis at Camp Crowder, Missouri. Geol Soc Am Abs 33 (6):132.

Gischler E, Gibson MA, Oschmann W (2008) Giant Holocene freshwater microbialites, Laguna Bacalar, Quintana Roo, Mexico. Sedimentology 55:1293–1309

Gondwe BRN, Lerer S, Stisen S, Marin L, Rebolledo-Vieyra M, Merediz-Alonso G, Bauer-Gottwein P (2010a) Hydrogeology of the south-eastern Yucatan Peninsula: new insights from water level measurements, geochemistry, geophysics and remote sensing. J Hydrol 389:1–17. doi:10.1016/j.jhydrol.2010.04.044

Gondwe BRN, Hong S-H, Wdowinski S, Bauer-Gottwein P (2010b) Hydrologic dynamics of the ground-water-dependent Sian Ka'an wetlands, Mexico, derived from InSAR and SAR data. Wetlands 30(1):1–13. doi:10.1007/s13157-009-0016-z

Gondwe BRN, Merediz-Alonso G, Bauer-Gottwein P (2011) The influence of conceptual model uncertainty on management decisions for a groundwater-dependent ecosystem in karst. J Hydrol. doi:10.1016/j.jhydrol.2011.01.023

Grajales-Nishimura JM, Cedillo-Pardo E, Rosales-Domínguez C, Morán-Zenteno DJ, Alvarez W, Claeys P, Ruíz-Morales J, García-Hernández J, Padilla-Avila P, Sánchez-Ríos A (2000) Chicxulub impact: the origin of reservoir and seal facies in the southeastern Mexico oil fields. Geol 28(4):307–310

Guérin R, Baltassat J-M, Boucher M, Chalikakis K, Galibert P-Y, Girard J-F, Plagnes V, Valois R (2009) Geophysical characterization of karstic networks: application to the Ouysse system (Poumeyssen, France). CR Geosci doi:10.1016/j.crte.2009.08.005

Gunn JD, Foss JE, Folan WJ, Carrasco MRD, Faust BB (2002) Bajo sediments and the hydraulic system of Calakmul, Campeche, Mexico. Anc Mesoam 13:297–315

Henson H, Sexton J, Henson M, Jones P (1997) Georadar investigation of karst in a limestone quarry near Anna. 67th Ann Int. Meet. SEG, Tulsa, OK, pp 763–767

Hildebrand AR, Penfield GT, Kring DA, Pilkington M, Camargo ZA, Jacobsen SB, Boynton WV (1991) Chicxulub crater: a possible Cretaceous/Tertiary boundary impact crater on the Yucatan Peninsula, Mexico. Geol 19:867–871

Huang H (2008) Airborne geophysical data leveling based on line-to-line correlations. Geophysics 73(3):F83–F89

Hung LQ, Batelaan O (2003) Environmental geological remote sensing and GIS analysis of tropical karst areas in Vietnam. Int Geosci and Remote Sens Symp 2003 (IGARSS '03). Proc IEEE Int 4:2964–2966

INEGI (1997) Carta edafológica [soil map]. Recursos electónicos. Escala 1:250,000. Shape file. Instituto Nacional de Estadística Geogrfía e Informática (INEGI), Aguascalientes, Mexico

ITC (2005) ILWIS 3.3 Academic. Software for remote sensing and GIS, International Institute for Geo-Information Science and Earth Observation (ITC), Enschede, The Netherlands

Kenkmann T, Schönian F (2006) Ries and Chicxulub: impact craters on Earth provide insights for Martian ejecta blankets. Meteorics Planet Sci 41(10):1587–1603

Kresic N (1995) Remote sensing of tectonic fabric controlling groundwater flow in Dinaric karst. Remote Sens Environ 53:85–90

Lara ME (1993) Divergent wrench faulting in the Belize southern lagoon: implications for Tertiary Caribbean plate movements and Quaternary reef distribution. Am Assoc Petrol Geol Bull 77:1041–1063

Li G, Loper DE, Kung R (2008) Contaminant sequestration in karstic aquifers: experiments and quantification. Water Resour Res 44:W02429. doi:10.1029/2006WR005797

Lopez-Ramos E (1975) Geological summary of the Yucatan Peninsula, chap 7. In: Nairn AEM, Stehli FG (eds) The ocean basins and margins, vol 3: the Gulf of Mexico and the Caribbean. Plenum, New York

Maathuis BHP, Wang L (2006) Digital elevation model based hydro-processing. Geocarto Int 21(1):21–26

Mangin A (1974) Contribution à l'étude hydrodynamique des aquifers karstiques [Contribution to the study of hydrodynamics in karst aquifers]. Ann Spéléol 29 (3):283–332; 29 (4):495–601; 30 (1):21–124

Marin LE, Perry EC, Essaid HI, Steinich B (2004) Hydrogeological investigations and numerical simulation of groundwater flow in the karstic aquifer of northwestern Yucatan, Mexico. In: Cheng A, H-D, Ouazar D (2004) Coastal aquifer management: monitoring, modeling and case studies. CRC, Boca Raton, FL, pp 257–278

Masoud A, Koike K (2006) Tectonic architecture through Landsat-7 ETM+/SRTM DEM-derived lineaments and relationship to the hydrogeologic setting in Siwa region, NW Egypt. J Afr Earth Sci 45:467–477

Miller TE (1996) Geologic and hydrologic controls on karst and cave development in Belize. J Cave Karst Stud 58(2):100–120

Mochales T, Casas AM, Pueyo EL, Pueyo O, Román MT, Pocoví A, Soriano MA, Ansón D (2008) Detection of underground cavities by combining gravity, magnetic and ground penetrating radar surveys: a case study from the Zaragoza area, NE Spain. Environ Geol 53:1067–1077. doi:10.1007/s00254-007-0733-7

Moore YH, Stoessell RK, Easley DH (1992) Fresh-water/sea-water relationship within a ground-water flow system, northeastern coast of the Yucatan Peninsula. Ground Water 30(3):343–350

Motschka K (2001) Aerogeophysics in Austria. Bull Geol Surv Jpn 52(2–3):83–88

NASA Landsat Program (1990) Tri-Decadal Landsat Orthorectified TM Mosaic of circa year 1990 (1985 to 1996) cloud-free images, N-16-15_loc. US Geological Survey, Sioux Falls, ID. Downloaded from http://glovis.usgs.gov/. Accessed 15 Jan 2010

NASA Landsat Program (2000) Landsat ETM+scenes p019r045_7x20000421, p019r046_7x20000421, p019r047_7x20000421, p020r045_7x20001106, p020r046_7x20001106, p020r047_7x20000327, p020r048_7x20000327. Orthorectified. US Geological Survey, Sioux Falls, ID, 14 Mar, 21 Apr, and 6 Nov 2000. Downloaded from http://glcf.umiacs.umd.edu/data/landsat/. Accessed 15 Jan 2010

NASA Landsat Program (2001) Landsat ETM+scene p020r046_7x20010314. Orthorectified. US Geological Survey, Sioux Falls, ID, 14 Mar 2001. Downloaded from http://glcf.umiacs.umd.edu/data/landsat/. Accessed 15 Jan 2010

NASA Landsat Program (2002) Landsat ETM+scene p019r048_7x20020918. Orthorectified. US Geological Survey, Sioux Falls, ID, 18 Sept 2002. Downloaded from http://glcf.umiacs.umd.edu/data/landsat/. Accessed 15 Jan 2010

Neuman BR, Rahbek ML (2007) Modeling the groundwater catchment of the Sian Ka'an Reserve, Quintana Roo. Assoc for Mex Cave Stud Bull 18AMCS, Austin, TX

Nyquist JE, Peake JS, Roth MJS (2007) Comparison of an optimized resistivity array with dipole-dipole soundings in karst terrain. Geophysics 72:F139

Ocampo AC, Pope KO, Fischer AG (1996) Ejecta blanket deposits of the Chicxulub crater from Albion Island, Belize. In: Ryder G, Fastovsky D, Gartner S (eds) The Creataceous-Tertiary event and other catastrophes in Earth history. Geol Soc Am Spec Pap 307:75–88

Ottowitz D (2009) 3-D Modellrechnung der Karststrukturen des Ox Bel Ha Höhlensystems zur Methodenevaluierung – Aeroelektromagnetic [3-D modeling of the airborne EM signal over the karstic caves of the Ox Bel Ha]. MSc Thesis, Univ. of Vienna, Austria

Paulsen DE, Lind IL (1997) Gammaspectral scanning of Creatceous/Tertiary boundary sections, Site 999 and Site 1001. Proc Ocean Drill Program Init Reps 165:7–13, 36, 186, 336

Perry E, Velazquez-Oliman G, Marin L (2002) The hydrogeochemistry of the karst aquifer system of the northern Yucatan Peninsula, Mexico. Int Geol Rev 44:191–221

Perry E, Paytan A, Pedersen B, Velazquez-Oliman G (2009) Groundwater geochemistry of the Yucatan Peninsula, Mexico: constraints on stratigraphy and hydrogeology. J Hydrol 367(1–2):27–40. doi:10.1016/j.jhydrol.2008.12.026

Peterson EW, Wicks CM (2005) Fluid and solute transport from a conduit to the matrix in a carbonate aquifer system. Math Geol 37(8):851–867. doi:10.1007/s11004-005-9211-5

PetRos EiKon (2008) GeoTutor IV, Emigma Version 6.4. Geophysical Forward Modelling Software, Orangeville, ON

Pope KO, Dahlin BH (1989) Ancient Maya wetland agriculture: new insights from ecological and remote sensing research. J Field Archeol 16(1):87–106

Pope KO, Ocampo AC, Duller CE (1991) Mexican site for K/T impact crater? J Nature 351:105

Pope KO, Ocampo AC, Fischer AG, Vega FJ, Ames DE, King Jr. DT, Fouke BW, Wachtman RJ, Kletetschka G (2005) Chicxulub impact ejecta deposits in southern Quintana Roo, México, and central Belize. In: Kenkmann T, Hörz F, Deutsch A (eds) Large meteorite impacts III. Geol Soc Am Spec Pap 384:171–190

Quintana Roo Speleological Society (QRSS) (2010) Survey and cartography of the underwater caves of Quintana Roo Mexico. http://www.caves.org/project/qrss/. Accessed 15 Jan 2010

Rebolledo-Vieyra M, Urrutia-Fucugauchi J, Marín LE, Trejo-García A, Sharpton VL, Soler-Arechalde AM (2000) UNAM scientific shallow-drilling program of the Chicxulub impact crater. Int Geol Rev 42:928–940

Refsgaard JC, van der Sluijs JP, Brown J, van der Keur P (2006) A framework for dealing with uncertainty due to model structure error. Adv Water Resour 29:1586–1597

Rosencrantz E (1990) Structure and tectonics of the Yucatan Basin, Caribbean Sea, as determined from seismic reflection studies. Tectonics 9(5):1037–1059

Schönian F, Stöffler D, Kenkmann T, Wittmann A (2004) The fluidized Chicxulub ejecta blanket, Mexico: implications for Mars. Poster, 35th Annual Lunar and Planet Sci Conf, League City, TX, March 2004

Schönian F, Tagle R, Stöffler D, Kenkmann T (2005) Geology of southern Quintana Roo (Mexico) and the Chicxulub ejecta blanket. Abstract no. 2389. 36th Annual Lunar and Planet Sci Conf, League City, TX, March 2005

SGM (2007) Carta geológica de México (Geological map of Mexico). Escala 1:2,000,000. 6a edición. Servicio Geológico Mexicano (SGM), Pachuca, Mexico

Shah SD, Smith BD, Clark AK, Kress WH (2008) A multi-tool geophysical and hydrogeological investigation of a karst aquifer system, Cibolo Canyon Development Area, Bexar County, Texas. In: Kuniansky E (ed) US Geol Surv Karst Interest Group Proc, Bowling Green, KY, May 2008, pp 107–116

Smart PL, Beddows PA, Coke J, Doerr S, Smith S, Whitaker FF (2006) Cave development on the Caribbean coast of the Yucatan Peninsula, Quintana Roo, Mexico. In: Harmon RS, Wicks C (eds) Perspectives on karst geomorphology, hydrology and geochemistry: a tribute volume to Derek C. Ford and William B. White. Geol Soc Am Spec Pap 404:105–128

Smith BD, Cain MJ, Clark AK, Moore DW, Faith JR, Hill PL (2005) Helicopter electromagnetic and magnetic survey data and maps, northern Bexar County, Texas. US Geol Surv Open-File Rep 05-1158, pp 122

Southworth CS (1985) Applications of remote-sensing data, eastern Yucatan. In: Ward WC, Weidie AE, Back W (eds) Geology and hydrogeology of the Yucatan and Quaternary geology of northeastern Yucatan Peninsula. New Orleans Geol Soc Publ, New Orleans, LA, pp 12–19

Steinich B, Marin LE (1996) Hydrogeological investigations in northwestern Yucatan, Mexico, using resistivity surveys. Ground Water 34(4):640–646

Steinich B, Marin LE (1997) Determination of flow characteristics in the aquifer of the Northwestern Peninsula of Yucatan, Mexico. J Hydrol 191:315–331

Supper R, Motschka K, Ahl A, Bauer-Gottwein P, Gondwe B, Merediz Alonso G, Römer A, Ottowitz D, Kinzelbach W (2009) Spatial mapping of submerged cave systems by means of airborne electromagnetics: an emerging technology to support protection of endangered karst aquifers. Near Surf Geophys 7 (5):613–627. doi:10.3997/1873-0604.2009008

Süzen ML, Toprak V (1998) Filtering of satellite images in geological lineament analyses: an application to a fault zone in central Turkey. Int J Remote Sens 19(6):1101–1114

Tam VT, De Smedt F, Batelaan O, Hung LQ, Dassargues A (2005) Study of cavernous underground conduits in Nam La (northwest Vietnam) by an integrative approach. Hydrogeol J 13:675–689. doi:10.1007/s10040-005-0452-7

Tulaczyk SM, Perry EC, Duller CE, Villasuso M (1993) Influence of the Holbox fracture zone on the karst geomorphology and hydrogeology of northern Quintana Roo, Yucatan Peninsula, Mexico. In: Beck BF (ed) Applied karst geology. Balkema, Rotterdam, The Netherlands, pp 181–189

Tun-Dzul FJ, Vester H, García RD, Schmook B (2008) Estructura arbórea y variabilidad temporal del NDVI en los "bajos inundables" de la Península de Yucatan, México [Forest structure and temporal variability of NDVI in the 'inundated lowlands' of the Yucatan Peninsula, Mexico]. Polibotánica 25:69–90

UBC-GIF (2000) A program library for forward modelling and inversion of frequency domain electromagnetic data over 1D structures, version 1.0. Developed by the UBC-Geophysical Inversion Facility, UBC, Vancouver, BC

Urrutia-Fucugauchi J, Marin L, Trejo-Garcia A (1996) UNAM Scientific drilling program of Chicxulub impact structure: evidence for a 300 kilometer crater diameter. Geophys Res Lett 23(13):1565–1568

Urrutia-Fucugauchi J, Morgan J, Stöffler D, Claeys P (2004) The Chicxulub Scientific Drilling Project (CSDP). Meteorics Planet Sci 39(5):787–790

Urrutia-Fucugauchi J, Chavez-Aguirre JM, Pérez-Cruz L, De la Rosa JL (2008) Impact ejecta and carbonate sequence in the eastern sector of the Chicxulub crater. C R Geosci 340:801–810

USGS (2006) Shuttle Radar Topography Mission, 3 Arc Second, Finished 2.0. US Geol Surv Glob Land Cover Facil, Univ of Maryland, College Park, MD

Vogelsang D (1987) Examples of electromagnetic prospecting for karst and fault systems. Geophys Prospect 35:604–617

Vouillamoz JM, Legchenko A, Albouy Y, Bakalowicz M, Baltassat JM, Al-Fares W (2003) Location of saturated karst aquifer with magnetic resonance sounding and resistivity imagery. Ground Water 41(5):578–586

Weidie AE (1985) Geology of Yucatan Platform. In: Ward WC, Weidie AE, Back W (eds) Geology and hydrogeology of the Yucatan and Quaternary geology of northeastern Yucatan Peninsula. New Orleans Geol Soc Publ, New Orleans, LA, pp 1–12

West GF, Macnae JC (1991) Physics of the electromagnetic induction exploration method. pp 5–45 In: Nabighian MN (ed) Electromagnetic methods in applied geophysics, vol 2: applications, part A and part B. SEG, Tulsa, OK

Worthington SRH (2003) A comprehensive strategy for understanding flow in carbonate aquifer. Speleogen Evol Karst Aquifers 1 (1):1–8

Zhdanov MS (2002) Geophysical inverse theory and regularization problems. Elsevier, Amsterdam